

# We are IntechOpen, the world's leading publisher of Open Access books Built by scientists, for scientists

6,900

Open access books available

186,000

International authors and editors

200M

Downloads

Our authors are among the

154

Countries delivered to

TOP 1%

most cited scientists

12.2%

Contributors from top 500 universities



WEB OF SCIENCE™

Selection of our books indexed in the Book Citation Index  
in Web of Science™ Core Collection (BKCI)

Interested in publishing with us?  
Contact [book.department@intechopen.com](mailto:book.department@intechopen.com)

Numbers displayed above are based on latest data collected.  
For more information visit [www.intechopen.com](http://www.intechopen.com)



# Multilayered and Chemiresistive Thin and Thick Film Gas Sensors for Air Quality Monitoring

*Tynee Bhowmick, Vibhav Ambardekar, Abhishek Ghosh, Moumita Dewan, Partha Pratim Bandyopadhyay, Sudip Nag and Subhasish Basu Majumder*

## Abstract

Selective detection of gases such as nitrogen dioxide ( $\text{NO}_2$ ), carbon monoxide (CO), carbon dioxide ( $\text{CO}_2$ ), and various volatile organic components (VOCs) is necessary for air quality monitoring. Detection of hydrogen ( $\text{H}_2$ ) is equally important as it is a flammable gas and poses serious threat of explosion when exposed to oxygen gas. We have studied the sensing characteristics of these gases using thin film deposited by chemical solution deposition as well as relatively thicker films deposited by atmospheric plasma spray (APS) process. The chapter starts with the sensing mechanism of chemiresistive sensors followed by the definition of gas sensing parameters. Subsequently, we have demonstrated selective  $\text{NO}_2$  sensing characteristics of zinc oxide-graphene (ZnO-G) multilayered thin film followed by CO and  $\text{H}_2$  sensing characteristics of ZnO thin film and  $\text{SnO}_2$  thick film. Cross-sensitivity among CO and  $\text{H}_2$  gases has been addressed through the analysis of conductance transients with the determination of activation energy,  $E_a$ , and heat of adsorption,  $Q$ . The concepts of reversible and irreversible sensing have also been discussed in relation to CO and  $\text{H}_2$  gases.  $\text{CO}_2$  sensing characteristics of  $\text{LaFe}_{0.8}\text{Co}_{0.2}\text{O}_3$  (LFCO)-ZnO thin film have been elucidated. Interference from CO has been addressed with principal component analyses and the ascertaining of  $E_a$  and  $Q$  values. Additionally, the variation of response with temperature for each gas was simulated to determine distinct parameters for the individual gases. Further, VOC sensing characteristics of copper oxide (CuO) thin film and  $\text{WO}_3$ - $\text{SnO}_2$  thick film were investigated. Principal component analysis was performed to discriminate the gases in CuO thin film. The interaction of  $\text{WO}_3$ - $\text{SnO}_2$  thick film with various VOCs was found to obey the Freundlich adsorption isotherm based on which  $E_a$  and  $Q$  values were determined.

**Keywords:** air quality monitoring, gas sensing, thin film sensor, thick film sensor, Langmuir adsorption isotherm, Freundlich adsorption isotherm, reversible sensing, irreversible sensing

## 1. Introduction

A recent surge in diseases related to poor air quality has made it mandatory to effectively monitor the level of harmful pollutants in the atmosphere. Poor

ventilation in indoor spaces as well as vehicular exhausts and emissions from industries poses serious threats to the quality of breathable air. Indoor air quality monitoring has become essential in order to counter the rising incidence of diseases such as sick building syndrome, which occurs in residential and office spaces due to poor ventilation. Indoor air pollutants are mostly volatile organic compounds (VOCs) which include alcohols such as ethanol and methanol and adverse pollutants such as benzene and formaldehyde. Other than this, carbon dioxide (CO<sub>2</sub>) and nitrogen dioxide (NO<sub>2</sub>) also pollute indoor living space [1].

Outdoor air quality is contaminated mainly due to the presence of carbon monoxide (CO), carbon dioxide, nitrogen oxides (NO<sub>x</sub>), sulfur dioxide (SO<sub>2</sub>), volatile organic compounds, and particulate matter. Urban sources of pollutants include vehicles and industries. In rural India, many people still use solid fuel such as wood, crop wastes, charcoal, and cow dung in open fires popularly known as “chulhas.” Such cooking practices are highly damaging to human health as they emit huge quantities of CO and NO<sub>2</sub> and cause an array of diseases including but not limited to pneumonia, stroke, heart disease, and lung cancer [2].

Air quality monitoring is thus mandatory to check the levels of various pollutants in the atmosphere. Agencies like Occupational Safety and Health Administration (OSHA) define the permissible exposure limits (PELs) of air pollutants to protect the health of workers. **Table 1** shows the permissible limit of various air contaminants.

Apart from these pollutants, detection of hydrogen (H<sub>2</sub>) gas is also important. It is used as fuel in space craft and rockets. It is reported that almost all CO sensing materials are cross-sensitive toward H<sub>2</sub> as well. It remains a major challenge to address the cross-sensitivity of CO sensor.

To detect these pollutants, one can use chemiresistive type thin or thick film oxide sensors, made from economic precursor materials. The use of oxide sensing materials in thin/thick film form has advantage over commonly used bulk Taguchi-type sensors. Thin/thick film sensors consume less power and also allow miniaturization of gas sensing systems.

The surface of oxide sensors acts as a catalyst to oxidize reducing pollutants (CO, H<sub>2</sub>, VOCs, etc.) to relatively benign gases (viz., CO forms CO<sub>2</sub>). Limited attempt has so far been made to study the gas sensing performance of oxide ceramics together with catalytic activity to oxidize the gas sensed [4]. For gas sensing performance, thin film sensor is preferred; however, for catalytic conversion, relatively thicker coating of oxide materials over a large area surface (often curved) is required.

Pollutant	Averaging time (h)	Level (ppm)
Carbon monoxide	8	35
Nitrogen dioxide	1	100
Carbon dioxide	8	5000
Sulfur dioxide	8	2
Ethanol	8	1000
Acetone	8	1000
Benzene	8	1
Formaldehyde	8	0.75

**Table 1.**  
OSHA permissible limit for various air pollutants [3].

Understanding of gas–solid interaction is of utmost importance to optimize the sensing performance of chemiresistive oxide sensors. Typically, Langmuir adsorption isotherm has been utilized to understand the resistance transients recorded upon exposing the oxide sensor to test gas environment. Through these kinetic analyses, interrelation among sensing layer thickness, its morphology, response %, sensitivity, and response/recovery times can be addressed adequately [5–7]. One can also estimate the adsorption and desorption energies of the test gas and reaction products, respectively. The estimated energies could be an effective tool to differentiate various types of test gases [7]. Base line stability of the sensing materials is also important to fabricate commercial sensing elements. Interrelation among the surface morphology, response time, and test gas concentration needs to be understood to fine-tune the base line stability [6, 8].

In view to the above, the primary goal of the present chapter is to describe a comprehensive approach to model the resistance/conductance transients based on Langmuir and Freundlich adsorption isotherms to address cross-sensitivity. Modeling the resistance/conductance transients allows us to estimate sensing parameters (such as response %, response/recovery time, etc.) and adsorption/desorption energies of test gas and reaction products. The estimated parameters help us to better understand the effect of the receptor (adsorption of gas molecule on sensing surface), transduction (electronic conduction pathway), and utility functions (effect of thickness and morphology of sensing materials) controlling the sensitivity, stability, and selectivity criteria of thin film type chemiresistive sensors.

The chapter is organized as follows: In the following sections, we have elucidated the mechanism of gas sensing followed by defining various sensing parameters. Subsequently we have briefed the dominant material characteristics influencing the sensing performance of thin film chemiresistive type gas sensors. Next, we have outlined the synthesis procedure of thin as well as thick film sensing elements. The synthesized materials were characterized in terms of their phase purity and microstructure evaluation. Finally, we have outlined the details of static as well as dynamic flow gas sensing measurements to investigate the sensing performance of the synthesized materials.

We have thus prepared thin and thick film sensors to detect NO<sub>2</sub>, CO, H<sub>2</sub>, CO<sub>2</sub>, and VOCs (ethanol, acetone, and isopropanol). Gas sensing mechanism has been described for each gas. Cross-sensitivity has been addressed through conductance transient analysis. The gas–solid interaction has been observed to follow either Langmuir or Freundlich adsorption characteristics. Based on this approach, the activation energy,  $E_a$ , and heat of adsorption,  $Q$ , were calculated to discriminate the gases. Stability of the gas sensors was also studied with respect to thin and thick films.

## **2. Salient features of semiconducting oxide gas sensor**

Semiconducting metal oxide (SMO) sensors are attractive for lower cost, smaller size, simpler operation principle, durability, and ease of fabrication together with their low concentration of gas detection limit [9]. These sensors change their conductivity when exposed to test gases of different concentrations [9]. However, the sensor operating temperature ( $\sim 300^\circ\text{C}$ ) needs to be lowered, and cross-sensitivity toward multiple gases needs to be minimized for its wide commercial adaptation. The operating principle and salient features of SMO-based chemiresistive sensors are briefly described as follows:

## 2.1 Principal of operation

For reducing CO gas sensing, **Figure 1** schematically illustrates the operative sensing mechanism. At elevated temperature, when the sensing film is exposed to air, the sensor surface provides active sites for the chemiadsorption of oxygen ions. Thus, oxygen adsorbs on to the sensor surface by accepting electrons from the conduction band of the sensing material. In the operating temperature ranging 100–500°C,  $O_2^-$ ,  $O^-$ , and  $O^{2-}$  are chemiadsorbed [10] forming an electron depletion layer (EDL). The EDL impedes grain to grain electron migration increasing the surface resistance for an “n”-type sensing material. When the sensor is exposed to a reducing gas such as CO or  $H_2$ , the adsorbed oxygen ions react with the test gas to release the electrons back to the conduction band of the sensing material. As a result the EDL width is reduced to decrease the surface resistance of the sensor.

In the case of a p-type sensor, since the majority carriers are holes, the oxidation reaction of the reducing test gas and the oxygen ions on the sensor surface would decrease the concentration of holes, increasing the sensor resistance. Assuming n-type and p-type sensors have similar morphologies, the response of p-type and n-type sensor is related by the following relation [11].

$$S_p = \sqrt{S_n} \quad (1)$$

where  $S_p$  is the gas response of p – type sensor and  $S_n$  is the gas response of n – type sensor.

## 2.2 Characteristic sensor parameters

**Figure 2** illustrates the characteristic sensor parameters one can estimate from the recorded resistance transient of an n-type sensor used for reducing gas sensing.

**Response (S) (%)**: Response is defined by the expression  $(R_a - R_g)/R_a \times 100$  or  $R_a/R_g$  where  $R_a$  and  $R_g$  are the measured resistances of the sensor exposed to air and test gas, respectively.

**Response time ( $\tau_{res}$ ) (s)**: Time required for a sensor to reach 90% of the maximum response on exposure to test gas [12].

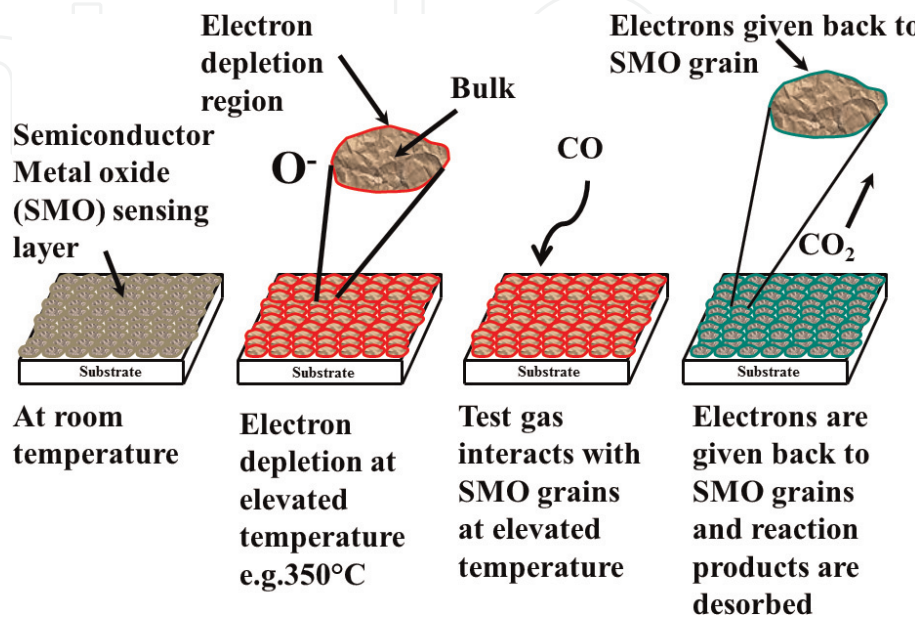


**Figure 1.**  
Gas sensing mechanism for a semiconducting metal oxide sensor.

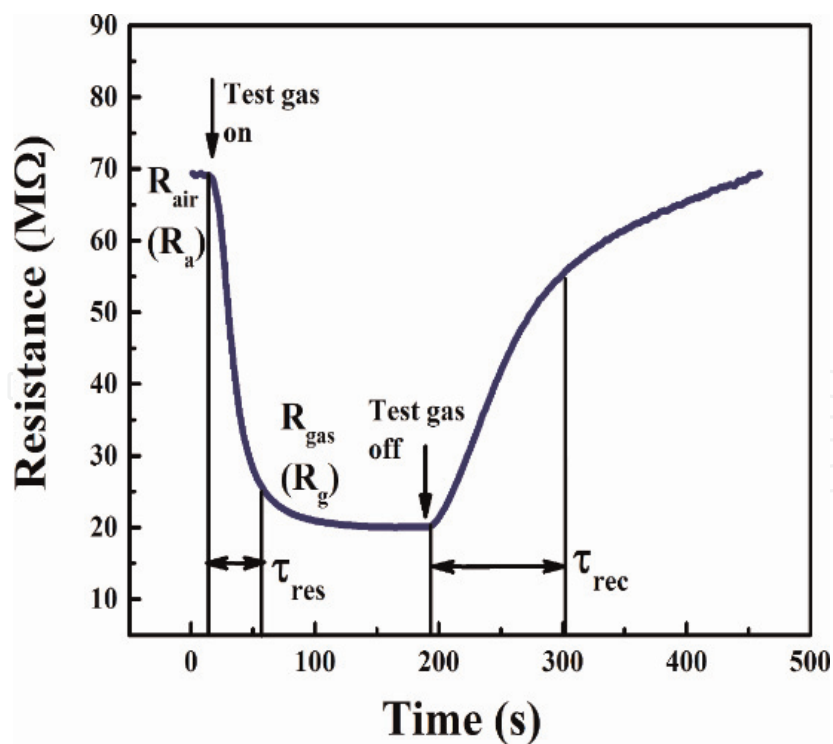


**Figure 2.**  
Resistance transient of an *n*-type gas sensor showing stable resistance in air ( $R_a$ ), stable resistance in gas ( $R_g$ ), response time ( $\tau_{res}$ ), and recovery time ( $\tau_{rec}$ ).

**Recovery time ( $\tau_{rec}$ ) (s):** Time required for a sensor to reach 90% of the original baseline resistance upon removal of the test gas.

**Optimum temperature ( $T_{opt}$ ) ( $^{\circ}\text{C}$ ):** The temperature at which the sensor exhibits maximum response.

**Selectivity:** The ability of a sensor to sense a selective gas preferentially among other test gases.

**Stability:** Minimum variation of sensor base resistance over a period of time.

**Sensitivity:** Change of measured signal (resistance, voltage or current) per analyte concentration unit [13].

### 2.3 Factors affecting gas sensing performance of thin film sensor

The sensing performance of SMO-based sensor is primarily influenced by the receptor, transducer, and utility functions of thin film sensing elements. The receptor function is influenced by the crystallite size of the sensing material, as at elevated temperature oxygen ions are chemiadsorbed on these crystallites forming a charge-depleted layer. The receptor function controls the interaction of test gases with the sensing elements. The transducer function controls the flow of charges between the electrodes. Finally the utility function controls the diffusion of gases. The parameters that regulate the receptor function of the sensor include composition of the material, surface to volume ratio, and size of the pores and grains. The transducer function is influenced by the grain to grain contact and the phase purity of the material. The composition of the material influences the defect chemistry which in turn changes the nature and concentration of the defects in the sensing material. The surface to volume ratio, pore size and grain size, and grain to grain contact of the sensing material are dependent on the growth condition.

Usually, the sintered block as well as thick film sensors consists of loosely sintered secondary particles made of innumerable tiny primary particles. Generally, the dimension of pores between the primary particles is in microns (termed as

macropores), whereas those in between the primary particles are in the order of nanometers ( $<50$  nm) (termed as mesopores). When the sensor is aged at elevated temperature, oxygen gas is diffused through both the macro- (corresponds to molecular diffusion) and mesoporous (corresponds to Knudsen diffusion) regions. Sensor particles are charge depleted due to chemiadsorption of oxygen. During gas sensing, the test gas diffuses through macro- and mesoporous regions and reacts with chemiadsorbed oxygen. The diffusion of gases through the mesoporous regions is known to play an important role during reducing gas sensing using semiconducting oxide-based sensing elements. For compact thin films, the gas-solid interaction mostly takes place at the geometric surface and to a limited extent along grain boundaries. In contrast, the active surface of the porous thin film is much larger than the compact thin films. In both these thin film structures, the key parameters that control the receptor function of the sensing element include its composition, nature of metal-oxygen bonding, specific surface area, porosity, and crystallite size. The transducer function is influenced by grain to grain contact and phase purity of the sensing element, and the utility function will be controlled by the gas diffusion either through grain boundaries or pores. For thin film sensing elements with pore size distribution in the range of 2–50 nm, Knudsen-type gas diffusion seems to be operative. Since the Knudsen diffusion coefficient is related to operating temperature, pore radius, molecular weight of the diffusing gas, and diffusion distance are related to film thickness; it is quite obvious that the sensing performance of a thin film sensor is related to the operating temperature, film thickness, and molecular weight of the test gas. Very limited attempt has so far been made to theoretically investigate the gas transport phenomena within the sensing film and correlate it with its sensing performance.

In the subsequent sections, we have outlined the sensing performance of ZnO-graphene multilayered thin films for  $\text{NO}_x$  sensing. Subsequently, CO and  $\text{H}_2$  sensing performance of ZnO thin film and  $\text{SnO}_2$  thick film were investigated. This was followed by  $\text{CO}_2$  sensing performance of 0.5% LFCO-ZnO thin film and VOC sensing characteristics of copper oxide (CuO) thin film and  $\text{WO}_3$ - $\text{SnO}_2$  thick film.

At constant sensor operating temperature, we assumed monolayer coverage of the reducing gas. Assuming Langmuir adsorption kinetics, we have theoretically predicted the response and recovery transients during gas sensing using thin and thick film sensing elements. From an application point of view, marginal base resistance drift of these thin film sensing elements is desirable during repeated response and recovery cycles. Often a significant drift in base line resistance is observed due to the partial recovery of thin and thick film sensing elements. For such partial recovery, the sensing is termed irreversible, whereas for reversible sensing, the base resistance is fully recovered. For a wide range of test gas concentrations and operating temperatures, the response transients of thin film sensing elements are modeled using Langmuir-Hinshelwood reaction mechanism. It is predicted that for irreversible-type sensing, the response time is reduced with the increase in test gas concentration, whereas for reversible sensing, response time is independent of the test gas concentration [12]. The  $\text{WO}_3$ - $\text{SnO}_2$  thick film sensor was modeled with Freundlich adsorption isotherm in which the concentration-dependent conductance was ascertained to be nonlinear.

### 3. Experimental

An economic wet chemical synthesis route was adopted to synthesize thin film gas sensing elements. Wet chemical synthesis is also energy efficient, and relatively cheaper precursor materials are used in wet chemical synthesis. We have

synthesized the ZnO-graphene (G) multilayer to study its NO<sub>2</sub> sensing characteristics. ZnO thin film sol was prepared by dissolving stoichiometric amount of zinc acetate dihydrate (Zn(CH<sub>3</sub>COO)<sub>2</sub>·2H<sub>2</sub>O) in 2-methoxyethanol (2-MOE) solvent with monoethanolamine (MEA) as stabilizer. The final concentration of the precursor solution was ~0.4 M/L. The precursor solution was heated at ~80°C for complete dissolution and stabilization. Graphene sheet from crystalline graphite was exfoliated by micromechanical cleavage using facile ultrasonication synthesis [14]. For this purpose, 5 mg of graphite powder was mixed in 5 ml of 2-MOE solution. N-methyl-2-pyrrolidine (NMP) solution was added for stabilization of the graphite sol. This suspension was then ultrasonicated for 3 h at room temperature and aged for 48 h. Multilayered ZnO-G thin films were fabricated by alternate deposition of ZnO and exfoliated graphite sol. Prior to sol deposition, the glass substrates were cleaned in trichloroethylene for 5 min followed by ultrasonic cleaning in the presence of acetone and deionized water. This was followed by drying of the substrates in flowing air. Details of deposition process have been reported elsewhere [14]. The multilayered films were annealed at 500°C for 1 h in air. The sensing performance of ZnO-G multilayered films were characterized using NO<sub>2</sub> (0.5–5.0 ppm), CO (50 and 500 ppm), H<sub>2</sub> (50 and 500 ppm), and i-C<sub>4</sub>H<sub>10</sub> (50 and 500 ppm) as test gases. The operating temperature was maintained in the range 100–200°C during gas sensing measurements. Additionally, mixed gas sensing behavior for the ZnO-G multilayered films has also been investigated using NO<sub>2</sub>/CO (5 ppm/50 ppm), NO<sub>2</sub>/H<sub>2</sub> (5 ppm/50 ppm), and NO<sub>2</sub>/i-C<sub>4</sub>H<sub>10</sub> (5 ppm/50 ppm) gas mixtures.

We have also studied the CO and H<sub>2</sub> sensing behavior of ZnO thin film and SnO<sub>2</sub> thick film. ZnO thin film was synthesized following the method described above. SnO<sub>2</sub> thick film was synthesized using a plasma spray deposition process. Commercial SnO<sub>2</sub> powder was used as feedstock material for the plasma spray process. Nitrogen (sans hydrogen) was used as the plasma forming gas and compressed air was used for cooling. Details of the process and equipment can be found elsewhere [7]. Alumina substrates (Ants Ceramic, India) were used for deposition as these are unaffected by the high temperatures generated during the atmospheric plasma spray process.

We have also studied the CO<sub>2</sub> sensing behavior of 0.5% LFCO (LaFe<sub>0.8</sub>Co<sub>0.2</sub>O<sub>3</sub>)-ZnO thin film composite. Lanthanum nitrate hexahydrate (La(NO<sub>3</sub>)<sub>3</sub>·6H<sub>2</sub>O), iron (III) nitrate nonahydrate (Fe(NO<sub>3</sub>)<sub>3</sub>·9H<sub>2</sub>O), and cobalt (II) nitrate hexahydrate (Co(NO<sub>3</sub>)<sub>2</sub>·6H<sub>2</sub>O) were dissolved in 2-MOE to prepare LFCO precursor sol with a final solution of 0.2 M via continuous stirring at room temperature. LFCO and ZnO sol were mixed in appropriate proportions to make composites of the composition xLFCO-(1-x) ZnO. The resulting sol was then spin coated on quartz substrate. Each layer was baked at 300°C with an intermittent heating interval of 10 min between layers to burn out the organic moieties. The coating and baking processes were repeated to yield films about 300nm thick. The resultant films were then annealed at 600°C for 2 h.

VOC sensing characteristics of CuO thin film and WO<sub>3</sub>-SnO<sub>2</sub> thick film were measured in a static gas sensing system. CuO sol (0.25 M) was synthesized using copper (II) acetate monohydrate (Cu(CH<sub>3</sub>COO)<sub>2</sub>·H<sub>2</sub>O) and 2-MOE as precursor materials. Glass substrates used for deposition were cleaned using trichloroethylene, acetone, and deionized water as described earlier. CuO sol was spin coated on glass substrates. Each layer was baked at 300°C for 5 min. The resultant film which was about 200 nm thick was annealed at 600°C for 1 hour to achieve complete crystallization. WO<sub>3</sub>-SnO<sub>2</sub> thick film composite was deposited on alumina substrates using a plasma spray deposition process. The feedstock material consists of WO<sub>3</sub> and SnO<sub>2</sub> powders in the weight ratio ~25:75. This ratio was found to be

optimum in a series of experiments with bulk pellets with various weight ratios (~25:75, 50:50, and 75:25) of  $\text{WO}_3$  and  $\text{SnO}_2$  [15].

The resistance change of the thin film sensing elements was measured using gold interdigitated electrode which was sputter coated onto the thin films using a dc sputter coater (Cressington 108, Ted Pella, Inc., USA). High-temperature silver paste was used as electrodes for the thick coatings. An indigenously developed dynamic gas sensing setup was used to measure the gas sensing characteristics of the thin films and thick plasma sprayed coatings. The gas sensing setup consists of a gas chamber connected to mass flow controllers (PR 4000, MKS Instruments, Germany) which control the flow rate of gases. The flow rate is calculated by the relation [12, 16].

$$C_{\text{mixed gas}} = \left[ C_{\text{test gas}} \times \frac{dV_{\text{test gas}}}{dt} \right] / \left[ \frac{dV_{\text{test gas}}}{dt} + \frac{dV_{\text{carrier gas}}}{dt} \right] \quad (2)$$

where  $C_{\text{test gas}}$  is the concentration of test gas,  $\frac{dV_{\text{test gas}}}{dt}$  is the flow rate of test gas, and  $\frac{dV_{\text{carrier gas}}}{dt}$  is the flow rate of carrier gas.

The temperature of the sensor inside the dynamic chamber is controlled with a temperature controller. An electrometer (6517 A, Keithley, USA) is connected to the sensor via gold-coated silver probes. Necessary voltage for electron migration between the grains of the sensor is controlled through the electrometer. The entire gas sensing setup is interfaced with a PC equipped with an RS-232 interface, GPIB card (National Instruments, USA), and LabVIEW 8.5 (National Instruments, USA) software [17]. A schematic of the mentioned gas sensing setup may be found in [12].

A static gas sensing set was employed to study the VOC (ethanol, acetone, and isopropanol) sensing characteristics of  $\text{CuO}$  thin film and  $\text{WO}_3\text{-SnO}_2$  thick film. Such a setup (also indigenous) consists of a rectangular chamber housing the sensor and the heater which is connected to the temperature controller [18]. The sensor is connected to a microcontroller which in turn is connected to the PC. Details of the system schematic may be found elsewhere [15]. Data (in this case, resistance) is collected at the rate of 1 bit/sec with the help of terminal emulation software. The sensor is heated to the temperature of operation and aged at that temperature to obtain a stable resistance ( $R_a$ ) which is followed by injection of gas. The resistance at which the sensor stabilizes in the presence of gas is termed  $R_g$ . The response of the sensor to the test gas is measured in terms of response percent which is defined as [19, 20].

$$\text{Response (S)\%} = \frac{|R_a - R_g|}{R_a} \times 100 \quad (3)$$

#### 4. Investigations on the gas sensing performance for air quality monitoring

Air quality monitoring involves the monitoring and quantification of various gases present in the atmosphere. Such gases include  $\text{NO}_x$  [21],  $\text{CO}$  [22],  $\text{CO}_2$  [23], and VOCs [24]. In addition, flammable gases such as  $\text{H}_2$  also need detection in order to prevent major disasters [25]. Apart from the detection of low concentration test gases, addressing the cross-sensitivity of the sensors also remains a major research issue. In addition to this, cost of air quality monitoring system is high, and efforts are needed to make it economic for wide uses. Keeping these considerations in mind, we have developed sensors to monitor these gases selectively. For

cross-sensitive sensing elements, necessary protocols are developed to address their selectivity. The sensing performances of synthesized sensing elements to detect test gases pertinent to air quality monitoring are described as follows.

4.1 NO<sub>2</sub> sensing

The main sources of NO<sub>2</sub> emissions are the incomplete burning of fuel and vehicular exhausts. According to a report in *The Hindu* [26], one of India’s premier newspapers, winter smog is caused in many parts of northern India due to burning of crop residue. An estimated 240 million tons of NO<sub>x</sub> (NO and NO<sub>2</sub>) is generated because of this practice. **Figure 3** shows percentage of NO<sub>x</sub> emissions in India from various sources. Other than this, vehicular exhausts also contribute to NO<sub>x</sub> formation. NO<sub>x</sub>, along with other pollutants such as SO<sub>2</sub>, VOCs, and particulate matter, forms smog as well as acid rain. These are markers of extremely polluted air and can have adverse health effect on humans.

Traditionally, semiconducting metal oxides such as SnO<sub>2</sub> [27], WO<sub>3</sub> [28], ZnO [29], etc. have been used for NO<sub>2</sub> sensing. Recently, composites such as Fe<sub>2</sub>O<sub>3</sub>-ZnO [30] has also gained prominence for selective NO<sub>2</sub> sensing. In addition, metal oxide (MO)-graphene (G) composites such as 0.5 wt%G-WO<sub>3</sub> [31] and SnO<sub>2</sub>-RGO [32] have also been reported as these sensors show high response at low operating temperature. These sensors are also highly selective.

Based on literature study (**Table 2**), we realized that MO-graphene (G) sensor will be an effective candidate for NO<sub>2</sub> sensing study. We have chosen the MO to be ZnO as it is an extremely stable sensor and can be easily modulated with graphene to operate at a low temperature. We have thus prepared a ZnO-G multilayer system

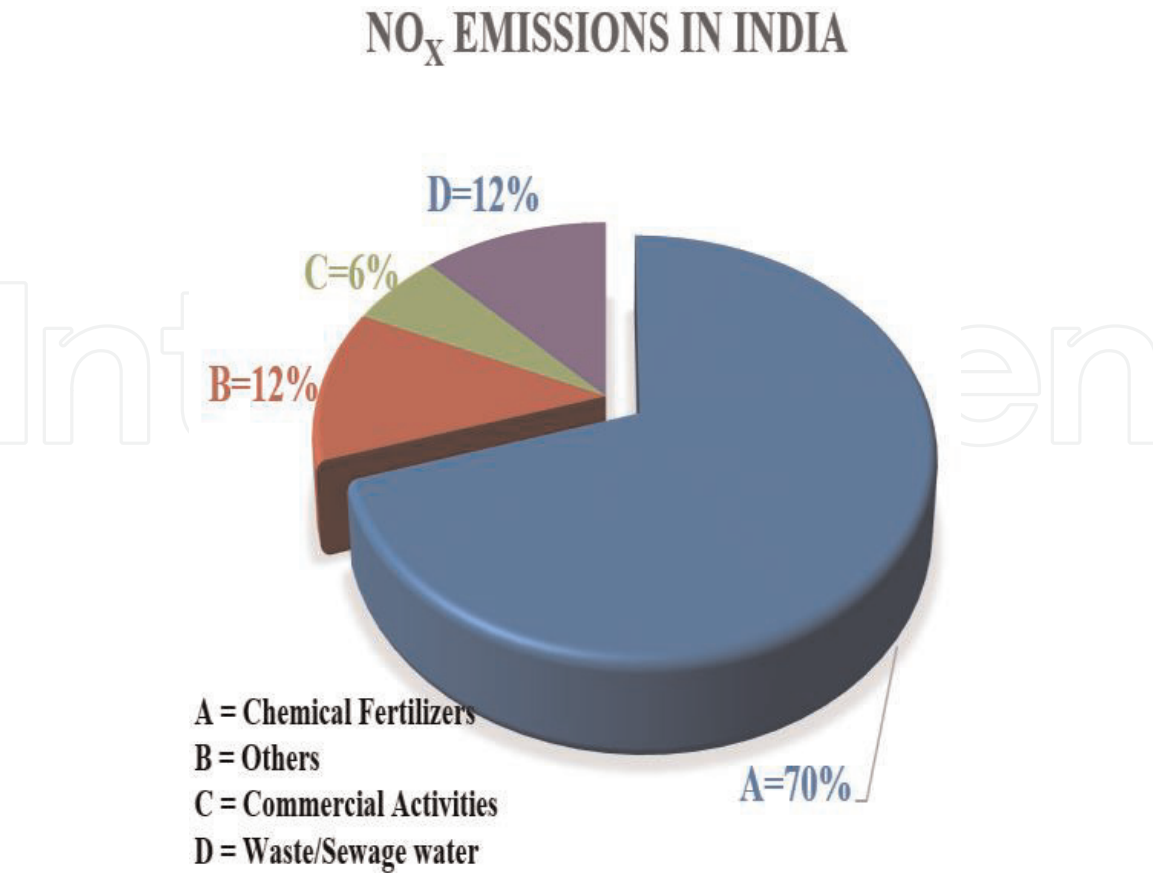


**Figure 3.** NO<sub>x</sub> emissions in India from various sources. Most of NO<sub>x</sub> emissions in India come from the use of chemical fertilizers in agriculture.

for NO<sub>2</sub> detection. We have measured NO<sub>2</sub> sensing with ZnO which is an n-type semiconductor. It shows optimum response of 26% to 5 ppm NO<sub>2</sub> at 150°C when the test temperature range is 100–200°C. Below 150°C, the response to NO<sub>2</sub> is almost negligible. However, with the addition of graphene to ZnO layers, the sensing response significantly increases to 894% [14]. These results are presented in **Figure 4**.

The response of ZnO-G multilayer thin film was also measured for 500 ppm H<sub>2</sub>, CO, and i-butane gases in the said temperature range. It was found that the response to 5 ppm NO<sub>2</sub> was far superior to any of the other gases. We have defined the selectivity ( $\kappa$ ) as

$$\kappa = \frac{S_{NO_2}}{S_{gas}} \tag{4}$$

where  $S_{NO_2}$  is the response % for NO<sub>2</sub> and  $S_{gas}$  is the response % for other gas (H<sub>2</sub>, CO, and i-butane).

The selectivity plot for NO<sub>2</sub> with respect to H<sub>2</sub>, CO, and i-butane has been shown in **Figure 5**. For all the gases, the selectivity factor  $\kappa$  has been found to be greater than 1. Thus we could detect NO<sub>2</sub> selectively in the presence of other gases.

Sensor material	Form	Gas	T <sub>opt</sub> (°C)	S%	Selectivity	$\tau_{res}, \tau_{rec}$ (s)	Conc. (ppm)	Ref.
SnO <sub>2</sub> -RGO	Nano powder	NO <sub>2</sub>	30	4.63 (R <sub>g</sub> /R <sub>a</sub> )	Yes	177, 510	5	[32]
SnO <sub>2</sub>	Hollow sphere	NO <sub>2</sub>	160	—	Yes	90, 25	5	[27]
0.5 wt%G-WO <sub>3</sub>	Nanopowder	NO <sub>2</sub>	RT, 250	1.96, 130 (R <sub>g</sub> /R <sub>a</sub> )	No	25–200	1, 5	[31]
ZnO	Nano powder	NO <sub>2</sub>	350	1.8 (R <sub>g</sub> /R <sub>a</sub> )	Yes	180, —	1	[29]
WO <sub>3</sub>	Thin film	NO <sub>2</sub>	300	70	No	—	10	[28]
Fe <sub>2</sub> O <sub>3</sub> -ZnO	Thin film	NO <sub>2</sub>	150	—	No	—	2.5	[30]
WO <sub>3</sub>	Thin film	NO <sub>2</sub>	300	87	Yes	300, 360	2	[33]
ZnO-G	Thin film	NO <sub>2</sub>	150	894	Yes	150, 315	5	[14]

**Table 2.**  
Comparison of the NO<sub>2</sub> sensing characteristics of various metal oxides.

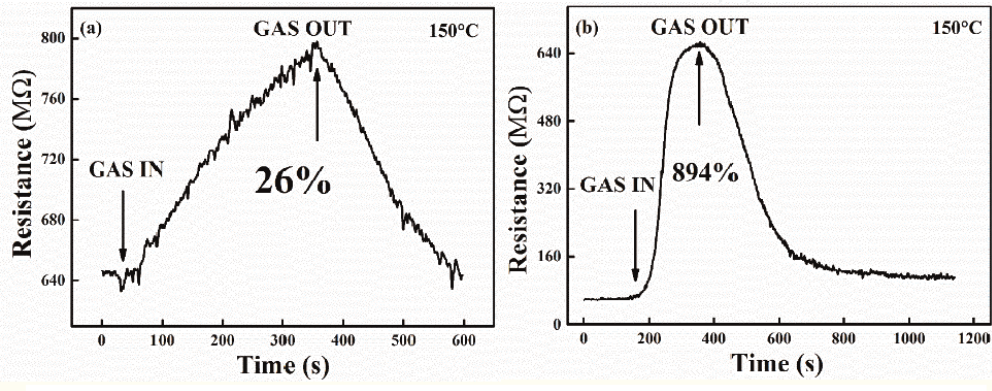


**Figure 4.**  
Resistance transients of (a) ZnO and (b) ZnO-G multilayer at 150°C. an enormous increase in response is observed on addition of graphene (Reprinted from [14] with the permission of AIP publishing).

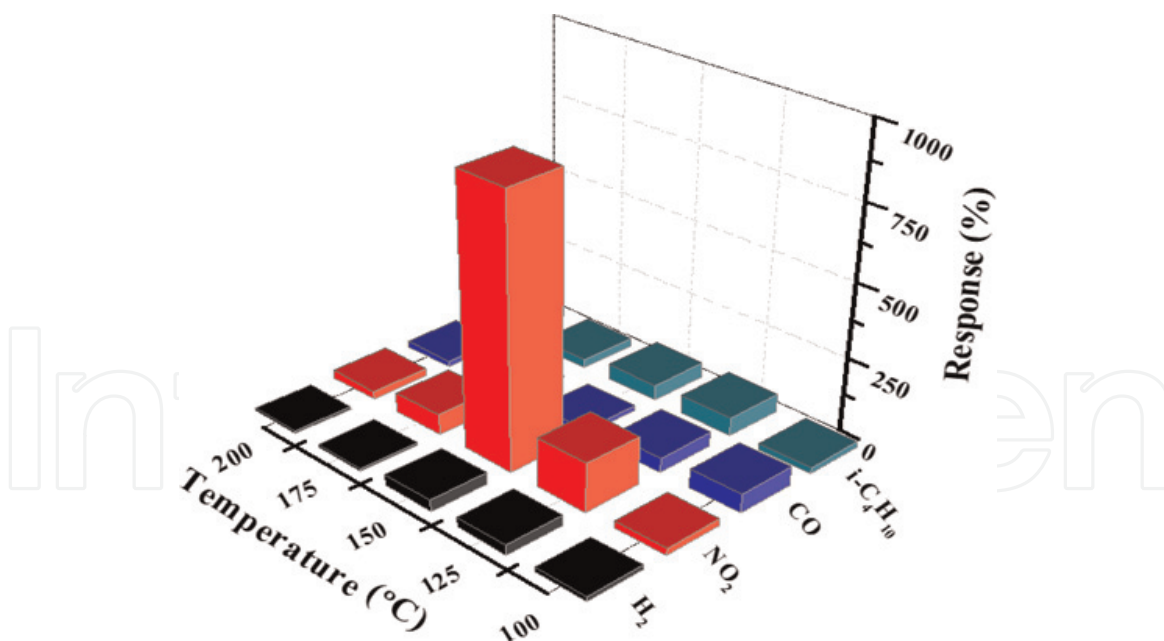
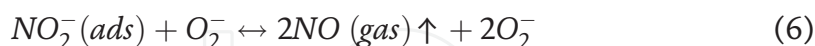
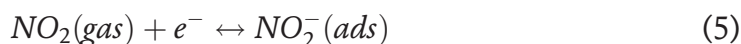


**Figure 5.**

Response % for 500 ppm *i*-butane, 500 ppm CO, 5 ppm NO<sub>2</sub>, and 500 ppm H<sub>2</sub> gases. Figure clearly shows the selective detection of NO<sub>2</sub> at 150°C (Reprinted from [14] with the permission of AIP publishing).

#### 4.1.1 NO<sub>2</sub> sensing mechanism

The significant enhancement in NO<sub>2</sub> sensing may be attributed to the formation of p-n junction between ZnO and graphene. In ZnO-G composite, graphene adheres to ZnO surface to increase the interaction with NO<sub>2</sub>. Due to the formation of p-n junction, electron flows from graphene to ZnO resulting in an electron-depleted surface. On exposure to air, majority of O<sub>2</sub><sup>-</sup> (dominant species at 150°C) species adsorb on to the ZnO-G surface, leading to the formation of electron-depleted layers. NO<sub>2</sub> reacts with this surface to form NO which is explained via the following equations:



The interaction of reducing gases (H<sub>2</sub>, CO and *i*-butane) with O<sub>2</sub><sup>-</sup> is poor at 150°C, thus leading to selective detection of NO<sub>2</sub>. A detailed figure of the sensing mechanism may be found in [14].

#### 4.1.2 Mixed gas sensing

We felt it important to sense NO<sub>2</sub> selectively in a mixed gas environment. Thus, the sensing performance of NO<sub>2</sub> was investigated in the presence of 5 ppm NO<sub>2</sub> and 50 ppm CO, 5 ppm NO<sub>2</sub> and 50 ppm *i*-butane, and 5 ppm NO<sub>2</sub> and 50 ppm H<sub>2</sub>. The response % histograms are presented in **Figure 6**. Principal component analyses (PCA) were used to address the cross-sensitivity. PCA involves the fast Fourier transforms (FFT) of the resistance transients of each gas (accomplished using MATLAB®, Mathworks, USA) which are fed into this unsupervised pattern recognition algorithm using STATISTICA-9, StatSoft, USA.

The plots between PC #1 and PC#2 are plotted separately in **Figure 7**. As shown in the inset of **Figure 7a**, distinct cluster forms among individual test gases (H<sub>2</sub>, CO, and *i*-C<sub>4</sub>H<sub>10</sub>). Also for NO<sub>2</sub>-CO, NO<sub>2</sub>-*i*-butane, and NO<sub>2</sub>-H<sub>2</sub> mixtures, distinct

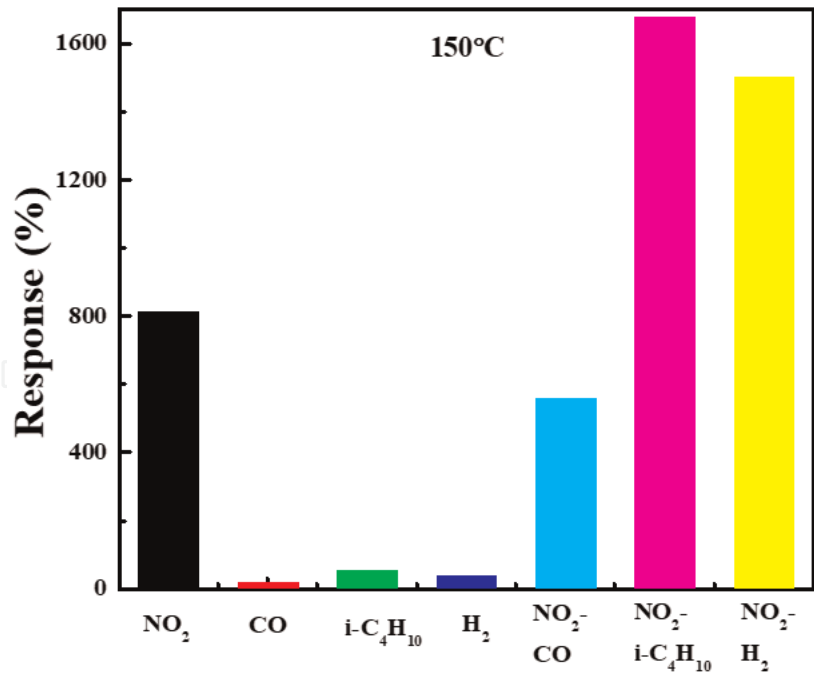


**Figure 6.** Gas sensing responses of individual NO<sub>2</sub>, CO, i-C<sub>4</sub>H<sub>10</sub>, and H<sub>2</sub> gases and mixed gas sensing for NO<sub>2</sub>/CO, NO<sub>2</sub>/i-butane, and NO<sub>2</sub>/H<sub>2</sub> (Reprinted from [14] with the permission of AIP publishing).

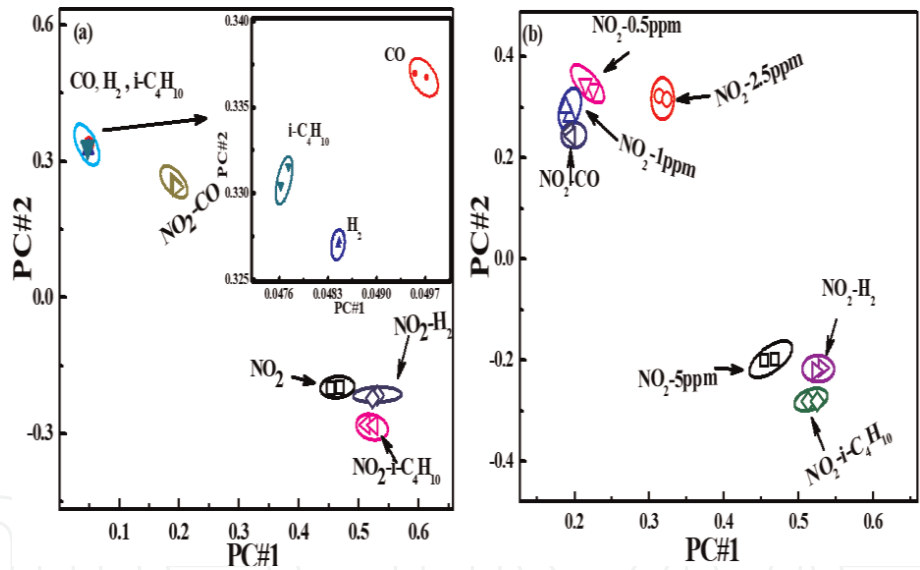


**Figure 7.** Principal component analysis of (a) NO<sub>2</sub>, CO, H<sub>2</sub>, i-C<sub>4</sub>H<sub>10</sub>, NO<sub>2</sub>-CO, NO<sub>2</sub>-H<sub>2</sub>, and NO<sub>2</sub>-i-C<sub>4</sub>H<sub>10</sub> gases and (b) mixed NO<sub>2</sub>/CO, NO<sub>2</sub>-H<sub>2</sub>, and NO<sub>2</sub>-i-C<sub>4</sub>H<sub>10</sub> gases and NO<sub>2</sub> gas varying NO<sub>2</sub> contents in the range 0.5–5 ppm measured at 150°C (Reprinted from [14] with the permission of AIP publishing).

clustering is readily identified in **Figure 7a**. PCA is also performed in mixed gases varying NO<sub>2</sub> contents in the range of 0.5–5 ppm (**Figure 7b**). Note that distinct clustering is also achieved in mixed gases with variable NO<sub>2</sub> contents, which eventually leads to successful differentiation between them.

**4.2 CO and H<sub>2</sub> sensing characteristics of thin and thick films**

Carbon monoxide is a major air pollutant. Open burning of wastes as well as fuel and biomass burning mainly in rural India is the main source of carbon monoxide. Additionally, fuel adulteration, especially in auto-rickshaws, also adds to the CO in air. On breathing CO-rich polluted air, one might end up inhaling CO as opposed to

oxygen. This CO then easily combines with the hemoglobin in blood forming carboxyhemoglobin, which reduces the oxygen-carrying capacity of blood. Additionally, tobacco smoke and heating appliances add to CO pollution of indoor air.

Hydrogen (H<sub>2</sub>) is a colorless, odorless, and tasteless gas. H<sub>2</sub> is also highly flammable with a low ignition energy (0.017 mJ) and low ignition temperature (~560° C). Hydrogen detection is critical to maintaining the safety of nuclear reactors where the reaction of water with high temperature core or cladding gives rise to evolution of hydrogen in radioactive waste tanks [34]. A small amount of H<sub>2</sub> is also produced as a result of methane explosions in coal mines [35]. H<sub>2</sub> is used as a liquid propellant for rockets as it is a zero emission fuel. It is also used in the reduction of metallic ores and for methanol production. H<sub>2</sub> has a lower explosive limit (LEL) of 4 vol % which makes its detection fairly crucial.

Semiconducting metal oxides such as SnO<sub>2</sub>, ZnO, WO<sub>3</sub>, etc. have demonstrated huge research potential when it comes to sensing of reducing gases such as hydrogen, carbon monoxide, hydrogen sulfide, ammonia, and VOCs. However, such materials exhibit poor selectivity, and efforts are on to achieve selectivity either by doping metal oxides or synthesis of composites. A brief review of literature (Table 3) suggests that selectivity has not been addressed for CO and H<sub>2</sub> sensing of metal oxides. We have synthesized ZnO thin film via spin coating process and SnO<sub>2</sub> thick film via plasma spray deposition process and studied their gas sensing characteristics with respect to H<sub>2</sub> and CO gases. We have analyzed the issue of selectivity through conductance transient analyses. The analyses have been performed for both thin and thick films for comparison. Additionally, we have discussed how stability varies in thin and thick film gas sensors when the test gases under consideration are the same.

ZnO thin film and SnO<sub>2</sub> thick film were investigated for H<sub>2</sub> and CO sensing characteristics in the temperature range 350–200°C. The concentration of each gas was fixed at 500 ppm. A maximum response of 68% for 500 ppm H<sub>2</sub> and 49% for 500 ppm CO was recorded at 300°C by ZnO thin film. SnO<sub>2</sub> thick film recorded maximum response to 500 ppm H<sub>2</sub> (81%) and 500 ppm CO (73%) at 250°C. Careful inspection of Figure 8 circumstantiates cross-sensitivity of H<sub>2</sub> and CO gases at all temperatures for both ZnO thin film and SnO<sub>2</sub> thick film sensors. This necessitates

Sensor material	Geometry	Gas	T <sub>opt</sub> (°C)	S%	Selectivity (w.r.t H <sub>2</sub> /CO)	τ <sub>res</sub> , τ <sub>rec</sub> (s)	Conc. (ppm)	Ref.
Sm <sub>2</sub> O <sub>3</sub>	Thick film	CO	250	1.4 (R <sub>g</sub> /R <sub>a</sub> )	No	35, 110	5	[36]
CuO	Nano-tube	CO	175	3.27 (R <sub>g</sub> /R <sub>a</sub> )	No	29, 37	1000	[37]
In <sub>2</sub> O <sub>3</sub>	Thin film	CO	350	45, 85 (R <sub>g</sub> /R <sub>a</sub> )	No	10– 50	1000	[38]
Pd-ZnO	Thin film	CO	150	—	No	17, 23	500	[39]
ZnO	Thin film	H <sub>2</sub>	300	21	No	58, 70	200	[40]
In-ZnO	Thin film	H <sub>2</sub>	300	65	No	35, 64	500	[41]
SnO <sub>2</sub>	Thin film	H <sub>2</sub>	350	83	No	23, 139	265	[42]
ZnO	Thin film	H <sub>2</sub>	400	23	Yes	110	1200	[43]
ZnO	Thin film	H <sub>2</sub>	300	68	Yes	53, 67	500	[9]
SnO <sub>2</sub>	Thick film	H <sub>2</sub>	250	80	Yes	30, 118	500	[7]

Table 3.  
Comparison of the CO and H<sub>2</sub> sensing characteristics of various semiconducting metal oxides.

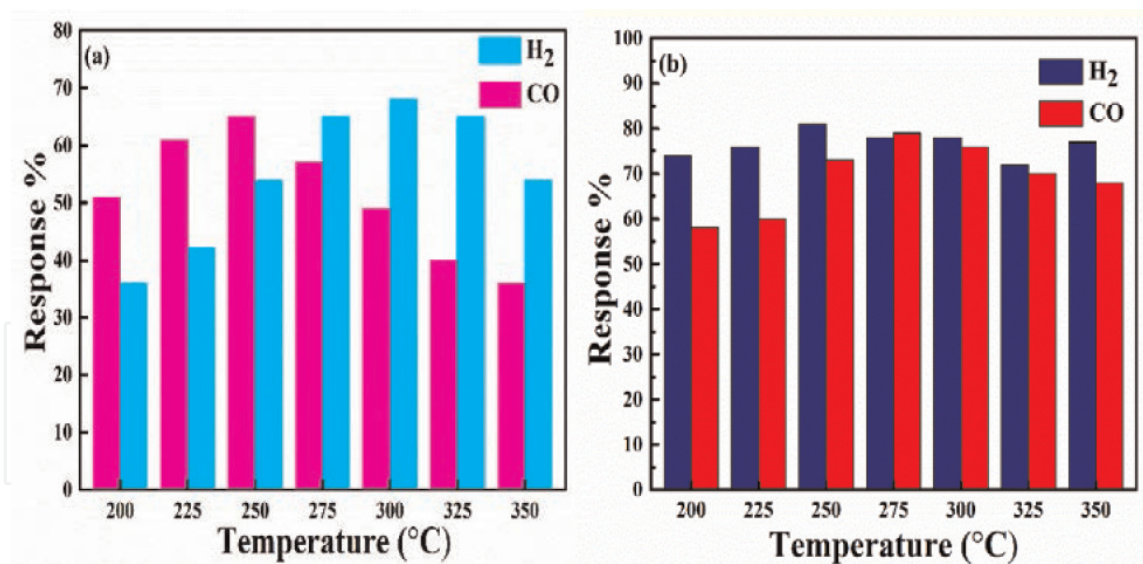


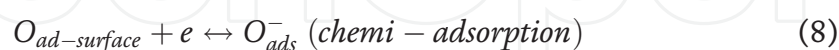
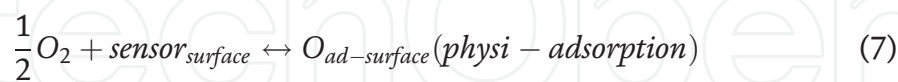
**Figure 8.**

Response % of (a) ZnO thin film and (b) SnO<sub>2</sub> thick film in response to 500 ppm H<sub>2</sub> and 500 ppm CO.

further analysis of the sensing data obtained. Analyses of conductance transients are a well-proven coherent technique to address the problem of cross-sensitivity. Although cross-sensitivity is shown by the sensors at all temperatures, we have performed mathematical analyses only for the optimum temperature of each kind of film. For H<sub>2</sub> and CO sensing, the recorded conductance transients of both ZnO (thin film) and SnO<sub>2</sub> (thick film) sensors were modeled using Langmuir adsorption kinetics [5].

#### 4.2.1 Analyses of conductance transients

In a preceding section, we have already outlined the sensing mechanism of n-type semiconducting sensor toward reducing gas sensing. Thus, ambient oxygen physisorbs on the sensor surface at ambient temperature (Eq. (7)). At elevated temperatures, the physisorbed oxygens are chemisorbed (Eq. (8)) by extracting electrons from semiconductor oxide grains. This creates an electron depletion layer (EDL) at the sensor surface [5, 10, 44, 45].



On exposing the sensor to a reducing gas, the chemisorbed oxygen reacts with the test gas (R) to yield oxidized reaction products. The reaction schemes and desorption of reaction product (RO<sub>gas</sub>) is described in Eqs. (9)–(11).



Among the cited relations, adsorption of oxygen ions and desorption of the reaction product (Eqs. (10) and (11)) are the rate-determining steps for response and recovery, respectively.

As discussed earlier, when the sensor is exposed to air, oxygen chemisorbs onto the sensor surface which results in the formation of an electron depletion layer (EDL). The EDL formed impedes the transfer of charge carriers from one grain to another. The relation between the height of this potential barrier and the conductance  $G$  of the sensor is given by the following Eq. (5):

$$G = G_0 \exp \left( -\frac{eV_s}{kT} \right) \quad (12)$$

where  $eV_s$  is the Schottky barrier,  $k$  is the Boltzmann constant, and  $T$  is the absolute temperature of operation of the sensor.

As the sensor is exposed to a reducing gas like CO or H<sub>2</sub>, the chemisorbed oxygen ions react with the gas to reduce the potential barrier between the grains, thus allowing the flow of electrons [46]. This process increases the conductance of the sensor.

The adsorption process of gas molecules on a solid surface was studied by Langmuir who developed an empirical model based on the surface coverage  $\theta$ . The Langmuir model assumes that (i) the surface on which the gas adsorbs is homogeneous, (ii) a specific number of sites are available for gas adsorption, and once all these sites are occupied, further adsorption is not possible. This is called monolayer adsorption, and (iii) all sites on which gas is adsorbed are equivalent in terms of heat of adsorption. Assuming the above, Langmuir formulated the equation below [5, 15].

$$\theta(t) = \frac{N(t)}{N^*} = A \left\{ 1 - \exp \left( -\frac{t}{t_A} \right) \right\} \quad (13)$$

where  $N(t)$  is the number of gas molecules adsorbed at time  $t$  and  $N^*$  is the total adsorption sites available, and

$$A \equiv \frac{P}{P + b} \quad (14)$$

where  $P$  is the gas pressure and  $b$  is related to heat of adsorption  $Q$  and is defined by the following relation:

$$b = b_0 \exp \left( -\frac{Q}{RT} \right) \quad (15)$$

$$b_0 = \frac{v}{K_0 \cdot S_{area} \cdot N_A} \times \sqrt{2\pi MRT} \quad (16)$$

where  $b_0$  is a constant,  $Q$  is the heat of adsorption ( $Q = E_d - E_a > 0$ ),  $E_a$  and  $E_d$  are the adsorption and desorption activation energies of gas molecules,  $R$  is the gas constant, and  $T$  is the operating temperature,  $T_{opt}$ . The pre-exponential constant  $b_0$  depends on  $v$  (frequency of oscillation of adsorbed molecules),  $K_0$  (fraction of those molecules with energy  $> E_A$ , adsorbed on surface),  $S_{area}$  (the surface area of a single adsorbed molecule),  $N_A$  (Avogadro number),  $M$  (molar mass of the gas), and  $R$  (the gas constant).

The amount of gas adsorption is dependent on the nature of the gas sensing surface, the operating temperature, and pressure of the gas. An adsorption isotherm is defined as the study of the amount of gas adsorption as a function of gas pressure. The simplest adsorption isotherm was given by Langmuir in which he assumes no

interaction between adsorbed atoms or molecules. At equilibrium, the rate of adsorption is equal to the rate of desorption. Thus, when  $t \rightarrow \infty$ ,

$$\theta = \frac{N(t)}{N^*} = A = \frac{P}{P + b} \quad (17)$$

Assuming a linear functional dependence between  $\theta(t)$  and conductance transient ( $G(t)$ ), the response behavior of the sensor that follows Langmuir model can be written as [5]

$$G(t)^{response} = G_0 + G_1 \left[ 1 - \exp \frac{-t}{\tau^{res}} \right] \quad (18)$$

where  $G_0$  is the base conductance of the sensor at time  $t = 0$ ,  $G_1$  is the fitting parameter, and  $\tau^{res}$  is the characteristic response time. This equation will only be valid if all three of Langmuir's criteria are satisfied.

$G_1$  in Eq. (18) is identical to  $A$  in Eq. (17); hence, at low gas concentration if we assume  $P \approx$  gas concentration ( $C$ ), we can then write

$$\frac{G_1}{1 - G_1} = \frac{C}{b} \quad (19)$$

If Langmuir adsorption isotherm is followed, then variation of  $G_1/(1-G_1)$  vs.  $C$  should be a linear fit and pass through the origin. The parameter  $b$  can be estimated from the slope of the plot.

Using Eq. (18), conductance transients during response at various concentrations for  $\text{SnO}_2$  sensing element for  $\text{H}_2$  and  $\text{CO}$  sensing were fitted to estimate values of  $G_0$ ,  $G_1$ , and  $\tau^{res}$ . **Figure 9a** shows the fitting of conductance transient of  $\text{SnO}_2$  thick film at  $250^\circ\text{C}$  in response to 500 ppm  $\text{H}_2$ . **Figure 9b** shows the variation of  $G_1/(1-G_1)$  with test gas concentration ( $C$ ) at  $250^\circ\text{C}$ . Since the linear fits for  $\text{H}_2$  and  $\text{CO}$  pass through the origin, Langmuir adsorption isotherm is satisfied [5, 47, 48]. The parameter  $b$  can be obtained from the inverse of the slope of the plot. Accordingly, the estimated 'b' values for  $\text{H}_2$  ( $1.5349 \times 10^{10}$  Pa) and  $\text{CO}$  ( $1.7834 \times 10^{11}$  Pa) have been determined from these plots [7]. From Eq. (15), expression for heat of adsorption ( $Q$ ) can be written as

$$Q = RT[\ln(b_0) - \ln(b)] \quad (20)$$

The molecular area of nitrogen is approximately  $16.2 \text{ \AA}^2$  as given in [49]. We have considered this as the area per site occupied by the test gas molecule ( $S_{area}$ ). Nitrogen has a molecular weight of  $28 \text{ g mole}^{-1}$  which gives  $S_{area} \sim 16.2 \text{ \AA}^2$ . A similar calculation for carbon monoxide with molecular weight  $28.01 \text{ g mole}^{-1}$  yields  $S_{area}$  to be  $\sim 16.2 \text{ \AA}^2$ . Assuming condensation coefficient  $K_o = 1$  [47],  $\nu = 10^{14} \text{ Hz}$  [49], and  $R = 8.314 \text{ JK}^{-1}$ ;  $b_o$  (at  $T \sim 523 \text{ K}$ ) can be estimated for  $\text{H}_2$  and  $\text{CO}$  gases using (Eq. (16)).

From the estimated values of  $b$  and  $b_o$ , heat of adsorption ( $Q$  in  $\text{J mol}^{-1}$ ) can be obtained for  $\text{H}_2$  and  $\text{CO}$  sensing using Eq. (20) [7].

$$Q_{\text{H}_2} = 23.418 \times 10^3 \text{ J mol}^{-1} = 23.418 \text{ KJ mol}^{-1} \quad (21)$$

$$Q_{\text{CO}} = 7.0138 \times 10^3 \text{ J mol}^{-1} = 7.0138 \text{ KJ mol}^{-1} \quad (22)$$

**Figure 9c** shows the plot of response time ( $\tau^{res}$ ) versus gas concentration ( $C$ ) on a logarithmic scale. As shown in **Figure 9c**, variation of  $\tau^{res}$  with  $C$  follows the following relation:

$$\tau^{res} = \tau_0 \times C^{-\beta} \tag{23}$$

The  $\ln \tau^{res}$  versus  $\ln C$  can be fitted linearly to estimate the rate constant and  $\beta$  for  $H_2$  and  $CO$  sensing where  $\tau_0$  is the fitting constant.

The temperature variation of  $\tau^{res}$  can be expressed by the following relation (47):

$$\tau^{res} = v^{-1} \times \exp \left( \frac{E_a + Q}{RT} \right) \tag{24}$$

From Eqs. (23) and (24), the value of  $E_a$  can be written as

$$E_a = RT \ln(\tau_0 \times C^{-\beta} \times v) - Q \tag{25}$$

The variation of  $E_a$  with concentration for  $H_2$  and  $CO$  gases is shown in **Figure 9d** [7]. The activation energy decreases from 134.3 kJ/mol to 131.8 kJ/mol for 500 ppm  $H_2$  to 50 ppm  $H_2$ , whereas the activation energy decreases from 151.05 kJ/mol to 150.07 kJ/mol and from 500 ppm  $CO$  to 50 ppm  $CO$  for  $SnO_2$  thick film sensor.

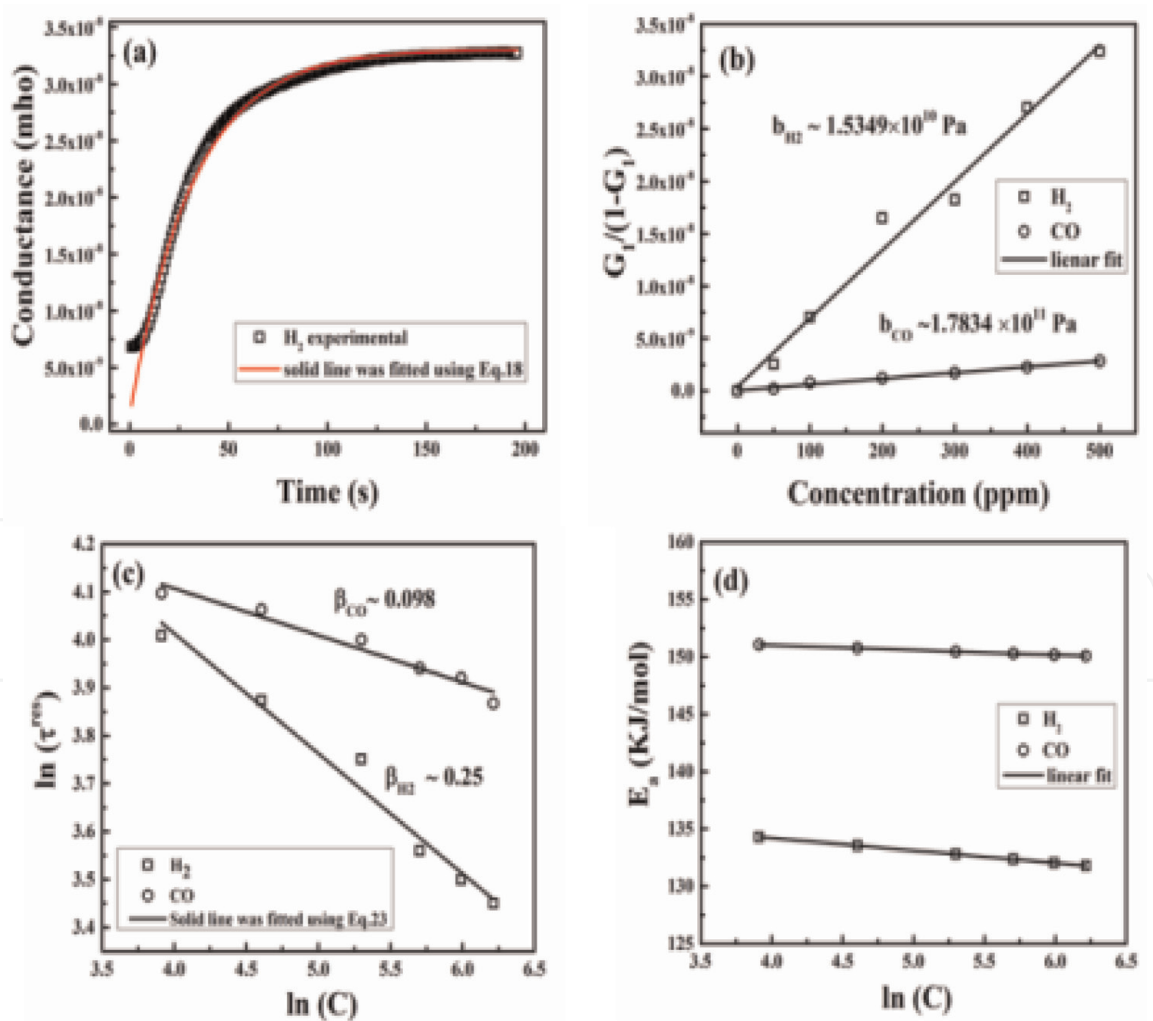


**Figure 9.**  
(a) Conductance transient plot for 500 ppm  $H_2$  sensing. Experimental points are shown by symbols, and the solid line was fitted using Eq. (18), (b) linear variation of  $G_1/(1-G_1)$  with concentration, (c) log-log plot of  $\tau^{res}$  with  $C$ . Experimental points are shown by symbols, and the solid line was fitted using Eq. (23), (d) variation of  $E_a$  with  $\ln C$  for  $H_2$  and  $CO$  sensing. For all these measurements, operating temperature was kept fixed at  $250^\circ\text{C}$  (**Figure 9a–d**, reprinted from [7] with permission from Elsevier).

Similar analyses for the *ZnO thin film sensor* yield activation energy values of 138.62 and 151.87 kJ/mol for 500 ppm  $H_2$  and CO, respectively. Activation energy increases with decreasing concentration for both the gases. The  $Q$  values for  $H_2$  and CO are 31.48 and 18.48 kJ/mol, respectively. Thus, the activation energy,  $E_a$ , and heat of adsorption,  $Q$ , may be used to differentiate  $H_2$  and CO gases for both thin and thick films.

#### 4.2.2 Stability of thin and thick film gas sensors

**Figure 10** shows the schematic of Langmuir-Hinshelwood mechanism [8] in which the oxygen as well as reducing test gas is initially adsorbed on the sensor surface shown by “A.” An oxidized reaction product is produced as a result of collision among adsorbed oxygen and reducing test species. For efficient formation of an oxidized reaction product “ $RO_{gas}$ ,” reducing test gas “ $R_{gas}$ ” (having concentration “ $C_g$ ”) and oxygen “O” should cross the energy barrier height shown by “TS” (transition state).

During this investigation, the sensing element was exposed to the test gas (during response) and air (during recovery), respectively. After removal of the test gas, it is expected that the sensor should switch back to the initial base resistance in air. Considering this fact, gas sensing can be classified into reversible and irreversible type. In reversible sensing, the base resistance is fully recovered, whereas for irreversible sensing, the base resistance recovers partially. The mechanism of reversible and irreversible sensing was reported elsewhere [8]. The irreversible sensing can be better understood from the gas–solid interaction. During gas sensor response process, CO and  $H_2$  gases are oxidized to  $CO_2$  and  $H_2O$ . These oxidized products are entrapped in the small pores of the sensing element. If the desorption of these products does not occur fully, the base resistance of the sensing element recovers partially. Therefore, a marginal drift in the baseline resistance is observed. The mathematical formulations of irreversible and reversible sensing are described in the subsequent sections.

##### 4.2.2.1 Irreversible sensing model

It is assumed that the site fraction  $\theta$  on the sensor surface is occupied by adsorbed oxygen ions  $O_{ad}^-$  and test gas ( $R_{gas}$ ) adsorption takes place over remaining available sites. For an “n”-type metal oxide semiconductor gas sensor, reducing gas reacts with chemiadsorbed oxygen to form an oxidized product as represented by Eq. (26).

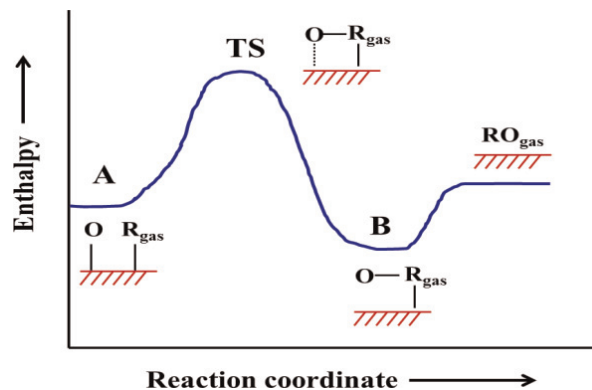


**Figure 10.**  
Schematic representation of Langmuir-Hinshelwood mechanism.



At constant operating temperature, it was assumed that the total number of active sites ( $F\theta$ ) can be expressed by the following relation:

$$\theta(\sim [O_{ad}^-]) + RO_{ad}(\text{occupied by } R_{gas}) = F\theta \quad (27)$$

It has been assumed that adsorption of the reaction product  $RO_{ad}$  takes place on the same sites over which reducing test gas ( $R_{gas}$ ) adsorbs initially. Since the formation of  $RO_{ad}$  is the rate-determining step for response process, sensor response is directly proportional to the formation of an oxidized reaction product  $RO_{ad}$ . Therefore, the sensor response during irreversible sensing can be expressed mathematically by the following relation:

$$\frac{d[RO_{ad}]}{dt} = k[O_{ad}^-]C_g \quad (28)$$

From Eq. (27), Eq. (28) can be written as

$$\frac{d[RO_{ad}]}{dt} = k[F\theta - RO_{ad}] * C_g \quad (29)$$

Integrating Eq. (29), we obtain

$$\int \frac{d[RO_{ad}]}{dt} = \int k[F\theta - RO_{ad}] * C_g \quad (30)$$

$$\int \frac{d[RO_{ad}]}{[F\theta - RO_{ad}]} = \int k * C_g * dt \quad (31)$$

Simplifying Eq. (31), we can write

$$-\ln[F\theta - RO_{ad}] = k * C_g * t + C \quad (32)$$

where C is the constant of integration.

$$\text{At } t \rightarrow 0, RO_{ad} \rightarrow 0 \text{ and } C = -\ln F\theta$$

Therefore Eq. (32) can be written as

$$-\ln[F\theta - RO_{ad}] = k * C_g * t - \ln F\theta \quad (33)$$

Simplifying Eq. (33), we can write

$$\ln \left[ 1 - \frac{RO_{ad}}{F\theta} \right] A = -k * C_g * t \quad (34)$$

Concentration of  $RO_{ad}$  at time t can be expressed as

$$[RO_{ad}](t) = F\theta[1 - \exp(-kC_g t)] \quad (35)$$

When all active sites ( $F\theta$ ) are adsorbed by the oxidized reaction product ( $RO_{ad}$ ), maximum sensor response is obtained. Therefore, the sensor response at a time t can be expressed by the following relation:

$$S(t) = S_{max} [1 - \exp(1 - kC_g t)] \quad (36)$$

$$S(t) = S_{max} [1 - \exp(-(t/\tau_{irrev}))] \quad (37)$$

where  $\tau_{irrev} = \frac{1}{kC_g}$  is termed as the characteristic response time (in seconds) during irreversible sensing.

#### 4.2.2.2 Reversible sensing model

In this case, the equilibrium constant for the sensing reaction (Eq. (38)) is termed as K, and the forward and reverse rate constants are k and k/K. The rate of change of  $RO_{ad}$  at time t can be written as

$$\frac{d[RO_{ad}]}{dt} = k[O_{ad}^-]C_g - k/K[RO_{ad}] \quad (38)$$

Rearranging Eq. (38),

$$\frac{d[RO_{ad}]}{k[F\theta]C_g - k[RO_{ad}](C_g + \frac{1}{K})} = dt \quad (39)$$

Simplifying Eq. (39), we can write

$$\frac{d[RO_{ad}]}{\left\{ \frac{[F\theta]C_g}{C_g + \frac{1}{K}} - [RO_{ad}] \right\}} = k \left( C_g + \frac{1}{K} \right) dt \quad (40)$$

Integrating Eq. (40), one can write

$$\int \frac{d[RO_{ad}]}{\left\{ \frac{[F\theta]C_g}{C_g + \frac{1}{K}} - [RO_{ad}] \right\}} = k \left( C_g + \frac{1}{K} \right) \int dt \quad (41)$$

Simplifying Eq. (41), one can write

$$-\ln \left\{ \frac{(F\theta)C_g}{(C_g + \frac{1}{K})} \right\} - [RO_{ad}] = k \left( C_g + \frac{1}{K} \right) t + C \quad (42)$$

$$\text{When } t \rightarrow 0, RO_{ad} \rightarrow 0, \text{ and } C = -\ln \left\{ \frac{(F\theta)C_g}{(C_g + \frac{1}{K})} \right\} \quad (43)$$

Therefore, Eq. (43) can be simplified as

$$-\ln \left\{ \frac{(F\theta)C_g}{(C_g + \frac{1}{K})} \right\} - [RO_{ad}] = k \left( C_g + \frac{1}{K} \right) t - \ln \left\{ \frac{(F\theta)C_g}{(C_g + \frac{1}{K})} \right\} \quad (44)$$

Eq. (44) can be simplified to

$$\ln \left[ \frac{\frac{(F\theta)C_g}{(C_g + \frac{1}{K})} - RO_{ad}}{\frac{(F\theta)C_g}{(C_g + \frac{1}{K})}} \right] A = -k \left( C_g + \frac{1}{K} \right) t \quad (45)$$

Eq. (45) can be further simplified to

$$1 - \frac{[RO_{ad}]}{\frac{(F\theta)C_g}{(C_g + \frac{1}{K})}} = \exp\left(-k\left(C_g + \frac{1}{K}\right)t\right) \quad (46)$$

The rate of change of  $RO_{ad}$  at time  $t$  can be written as

$$[RO_{ad}](t) = \left\{ \frac{(F\theta)C_g}{(C_g + \frac{1}{K})} \right\} \left\{ 1 - \exp\left(-k\left(C_g + \frac{1}{K}\right)t\right) \right\} \quad (47)$$

$$[RO_{ad}](t) = \left\{ \frac{(F\theta)C_g K}{(1 + C_g K)} \right\} \left\{ 1 - \exp - \left\{ (1 + C_g K)/K \right\} kt \right\} \quad (48)$$

Sensor response ( $S(t)$ ) can be written as

$$S(t) = S_{max} \left\{ \frac{C_g K}{(1 + C_g K)} \right\} \left\{ 1 - \exp - \left\{ (1 + C_g K)/K \right\} kt \right\} \quad (49)$$

Assuming  $1 + C_g K \approx C_g K$ , one can write

$$S(t) = S_{max} [1 - \exp(-t/\tau_{rev})] \quad (50)$$

where  $\tau_{rev}$  is the characteristic response time during reversible sensing.

**Figure 11a, b** shows the concentration-dependent resistance transients for  $H_2$  and CO sensing for ZnO thin film. These measurements were taken at  $300^\circ\text{C}$  by varying the test gas concentration. During these measurements, drift in baseline resistance was observed as shown by the dashed line in **Figure 11a, b**. Therefore, time-dependent response % for  $H_2$  and CO sensing was fitted using irreversible sensing model as given in Eq. (37). **Figure 11c** shows the typical response % vs. time fitting for 500 ppm  $H_2$  and CO sensing. Inset of **Figure 11c** represents variation of  $\tau_{irrev}$  (in seconds) with concentration (in ppm) in which  $\tau_{irrev}$  decreases systematically with increase in test gas concentration which is a typical behavior in case of irreversible gas sensing as reported by [8].

We have also investigated the reversible sensing behavior of plasma sprayed  $\text{SnO}_2$  thick film sensor [7]. The  $\text{SnO}_2$  thick film sensor shows marginal drift in baseline resistance when exposed to 20–500 ppm CO and  $H_2$ . This is shown in **Figure 12**.

Inset of **Figure 12c** shows the variation of characteristic response time  $\tau_{rev}$  (s) with concentration (ppm).  $\tau_{rev}$  was almost invariant of the test gas concentration in the range 500–200 ppm. Interestingly,  $\tau_{rev}$  was also invariant of test gas concentration in the range 100–20 ppm. However, the value of  $\tau_{rev}$  was found to be higher in the lower concentration range (100–20 ppm) than that of the higher concentration range (500–200 ppm).

**Figure 13** shows the surface micrograph for (a) ZnO thin film and (b)  $\text{SnO}_2$  thick film sensing elements. ZnO thin film exhibits denser surface morphology than  $\text{SnO}_2$  thick film as revealed from **Figure 13a**. In line with this discussion, irreversible sensing behavior for ZnO thin film can be attributed to denser surface morphology. It may be noted here that our results for ZnO thin film are in accordance with [8]. On the other hand, reversible sensing behavior in case of  $\text{SnO}_2$  thick film can be attributed to its porous surface morphology as revealed from **Figure 13b**.

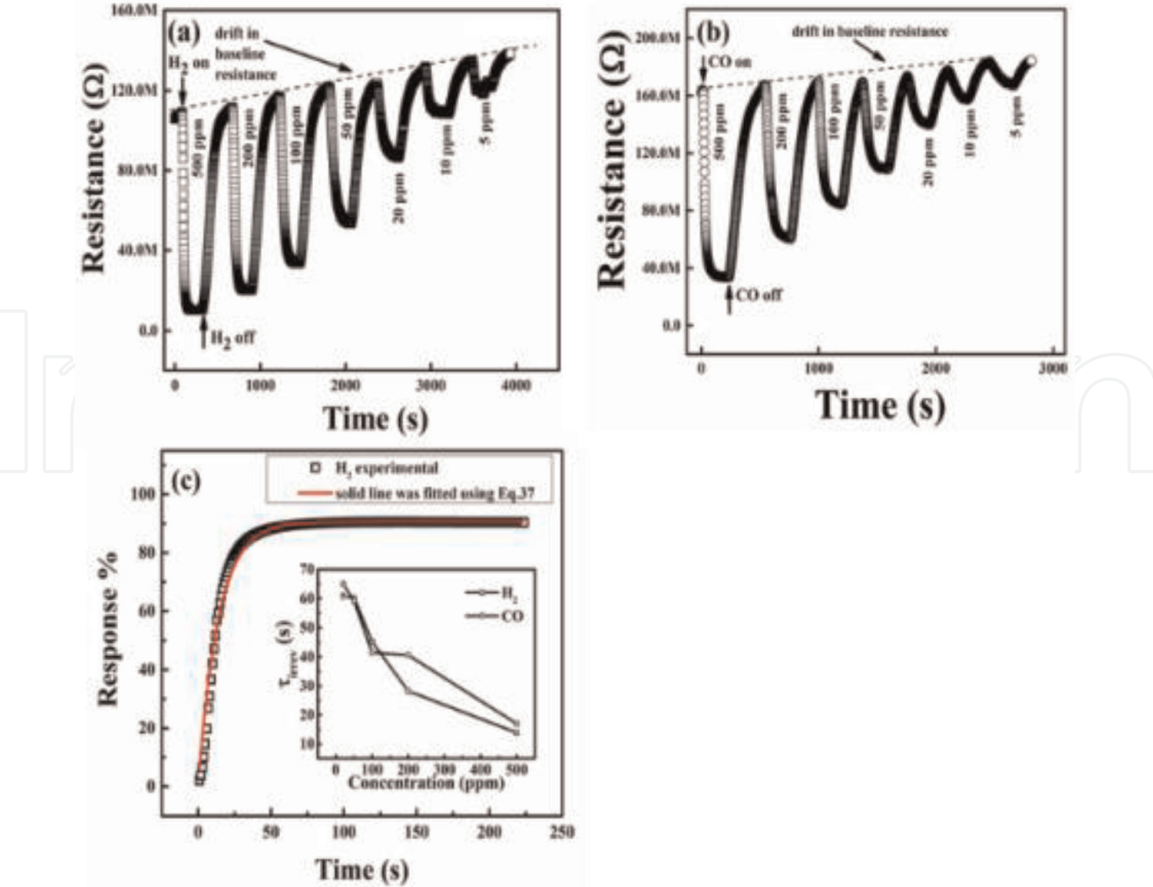


**Figure 11.** Concentration-dependent resistance transients recorded at 300°C for (a) H<sub>2</sub>, (b) CO, (c) time-dependent response % fitting for 500 ppm H<sub>2</sub> sensing for ZnO thin film. Experimental points (symbols) and the solid line were fitted using Eq. (37). Inset shows the variation of  $\tau_{rev}$  with concentration.

### 4.3 CO<sub>2</sub> sensing characteristics

Carbon dioxide concentrations have increased enormously in the atmosphere in the past hundred years or so. In the preindustrial era, CO<sub>2</sub> concentration was ~280 ppm. However, current global standards put CO<sub>2</sub> concentrations at an alarming level of 400 ppm mainly arising from deforestation and the burning of fossil fuels. India alone emitted 2299 million tons of CO<sub>2</sub> in 2018 according to an International Energy Agency (IEA) report [50]. Most of India's emissions come from the burning of coal. Increased CO<sub>2</sub> emissions have led to global warming—a climate phenomenon that is responsible for the increasing number of storms as well as droughts [51]. In addition, increased levels of CO<sub>2</sub> in the atmosphere affect human health severely. **Table 4** summarizes the effects on human health with increasing CO<sub>2</sub> concentrations. It is thus incumbent that we take necessary steps to detect CO<sub>2</sub> concentrations in the atmosphere.

Research on CO<sub>2</sub> sensing gained prominence in the late 1980s when researchers such as Toshio Maruyama [52] and Yasuhiro Shimizu [53] reported a NASICON (Na<sub>3</sub>Zr<sub>2</sub>Si<sub>2</sub>PO<sub>12</sub>)-based solid electrolyte gas sensor and an electrochemical K<sub>2</sub>CO<sub>3</sub>-polyethylene glycol CO<sub>2</sub> sensor, respectively. However, it was soon realized that handling these materials was cumbersome and incorporating these into actual devices posed a serious challenge. Research was thus shifted to resistive-type sensors [54, 55] which were far better in terms of stability and could be easily miniaturized to accommodate in sensing devices. However, such sensors were plagued with poor selectivity and low response to CO<sub>2</sub>. This prompted the use of mixed

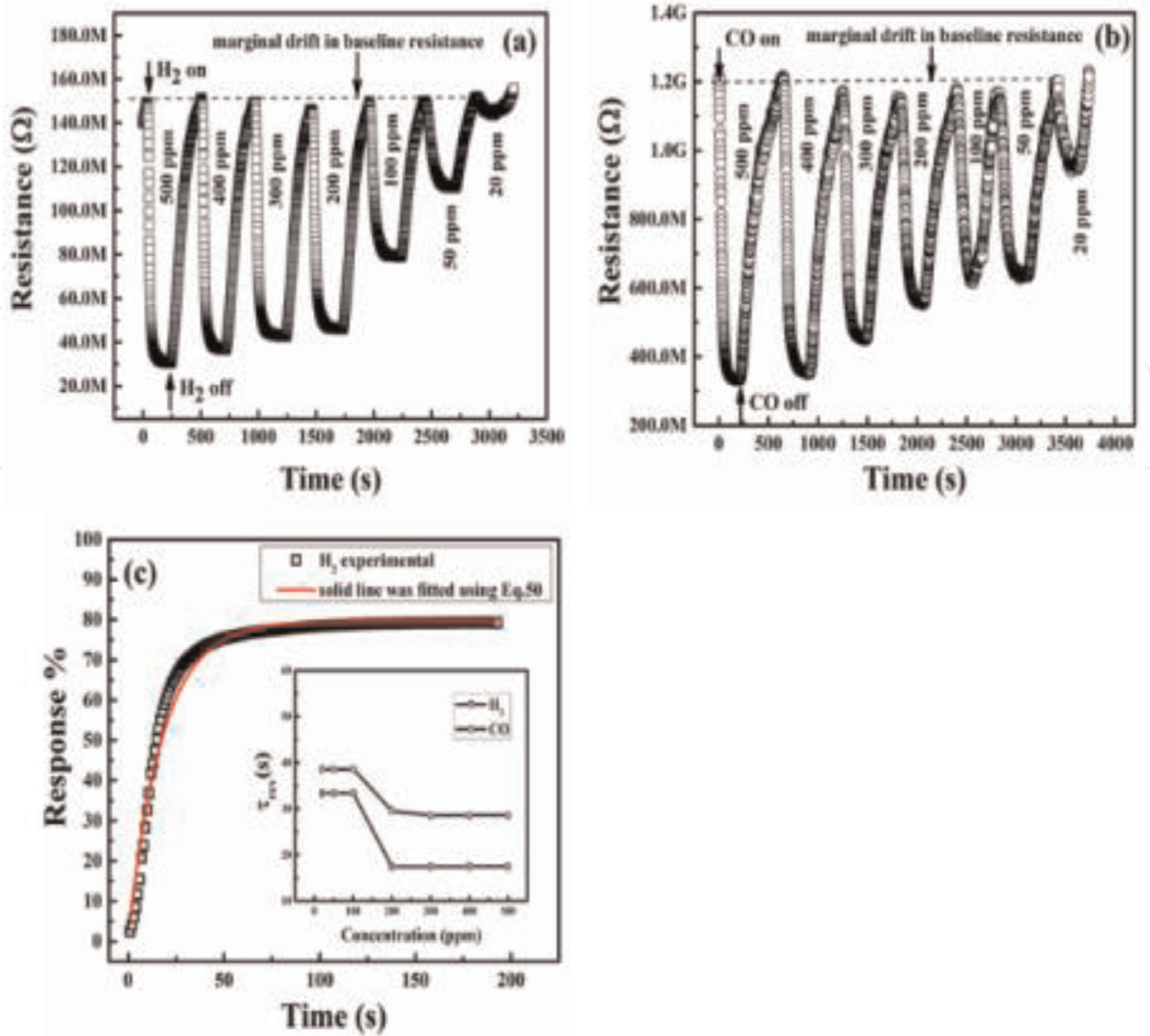


**Figure 12.** Concentration-dependent resistance transients recorded at 250°C for (a) H<sub>2</sub>, (b) CO, and (c) time-dependent response % fitting for 500 ppm H<sub>2</sub> sensing. Experimental points (symbols) and the solid line were fitted using Eq. (50). Inset shows the variation of  $\tau_{rev}$  with concentration (Figure 12a–c has been reprinted from [7] with permission from Elsevier).

oxide or composite sensors [56–58], the research potential of which is still being investigated [59, 60].

A comprehensive study of literature (elaborated in **Table 5**) related to CO<sub>2</sub> sensing leads us to the fact that formation of p-n junctions is an important criterion for CO<sub>2</sub> detection. We have reported CO<sub>2</sub> sensing of ~36% achieved using a LFCO-ZnO composite thin film.

CO<sub>2</sub> sensing characteristics of LFCO-ZnO composite thin film was measured in the temperature range 350–150°C. The highest response of ~36% was obtained at 300°C to 2500 ppm CO<sub>2</sub>, and the response decreases to 12% at 150°C. The response and recovery times recorded at 300°C are 300 and 630 s, respectively. The composite shows n-type sensing behavior which confirms the dominance of ZnO crystallites [67]. The LFCO-ZnO thin film composite is cross-sensitive to CO<sub>2</sub>. A response of 65% was recorded for 500 ppm CO at 300°C. The composite shows higher response to both CO and CO<sub>2</sub> than pure LFCO and ZnO thin films. To address the cross-sensitivity of the composite thin film, principal component analysis of the resistance transients was performed. The relevant features of the resistance transients of the test gases are extracted using fast Fourier transform technique. These features are then used as input parameters for PCA.

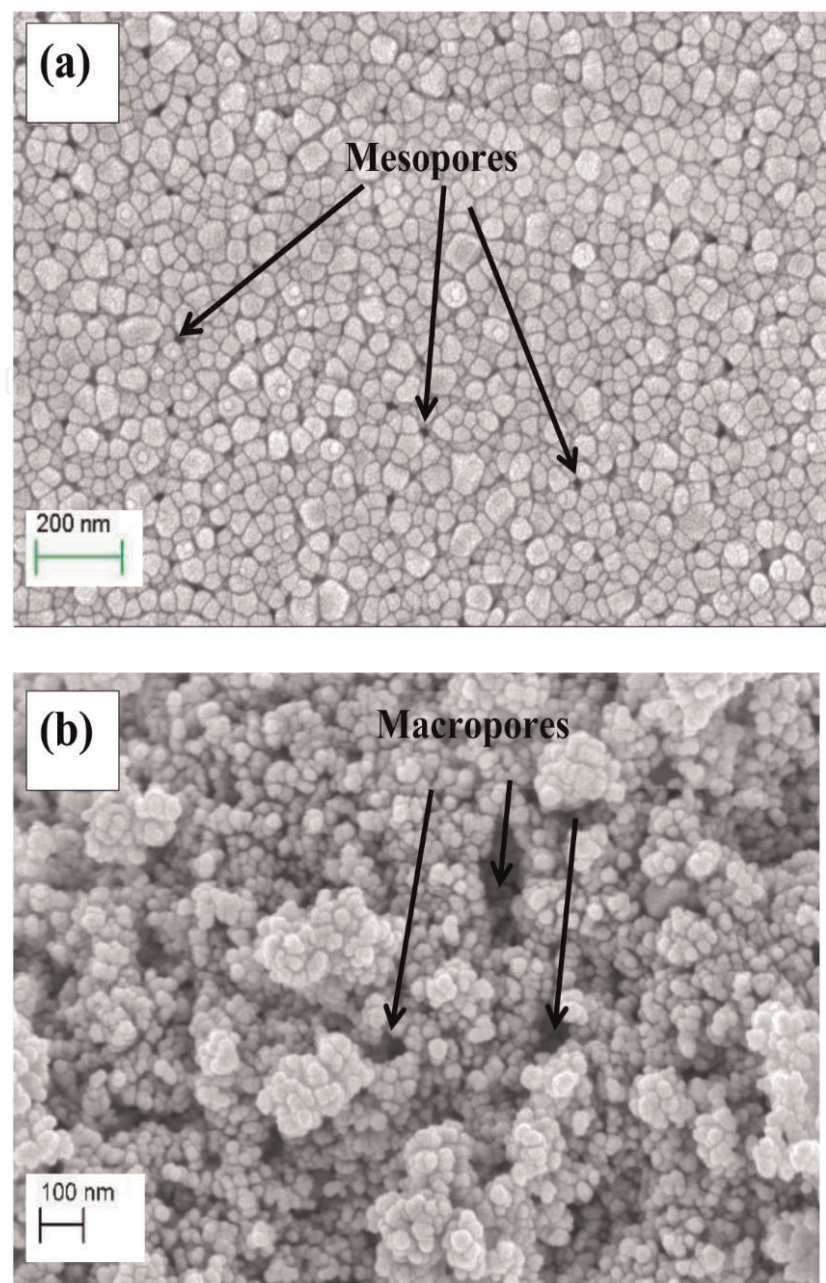


**Figure 13.**  
Surface micrograph: (a) ZnO thin film and (b) SnO<sub>2</sub> thick film.

Concentration of CO <sub>2</sub> (ppm)	Effect on human health
250–300	Normal outdoor air
350–1000	Indoor air
100–2000	Drowsiness (poor air)
2000–5000	Increased heart rate, nausea, headaches
>5000	Oxygen deprivation begins
>40,000	Serious oxygen deprivation leading to brain damage, coma, and death

**Table 4.**  
Effect on human health with increasing concentrations of CO<sub>2</sub>.

**Figure 14d** shows low dispersion of CO and CO<sub>2</sub> for the LFCO-ZnO composite thin film after performing PCA. Thus, FFT-PCA is an efficient tool for the differentiation of CO and CO<sub>2</sub> gases for LFCO-ZnO thin film.

Sensor material	Form	Gas	T <sub>opt</sub> (°C)	S%	Selectivity	τ <sub>res</sub> , τ <sub>rec</sub> (s)	Conc. (ppm)	Ref.
ZHS microcubes on ZnO nanorods	Thin film	CO <sub>2</sub>	150	354	No	10, 24	2500	[61]
LaBaCo <sub>2</sub> O <sub>5+δ</sub>	Bulk	CO <sub>2</sub>	300	1.04 (R <sub>g</sub> /R <sub>a</sub> )	No	—	400	[62]
Graphene sheet	Thin film	CO <sub>2</sub>	60	26	No	8, 10	100	[63]
BaCO <sub>3</sub> -Co <sub>3</sub> O <sub>4</sub>	Bulk	CO <sub>2</sub>	150	15	No	227, 245	10,000	[59]
Ag/BaTiO <sub>3</sub> -CuO	Thin film	CO <sub>2</sub>	250	28	No	900, 600	5000	[64]
Ca/Al-doped ZnO	Bulk	CO <sub>2</sub>	300	15	No	—	2500	[65]
LaFeO <sub>3</sub> -SnO <sub>2</sub>	Bulk	CO <sub>2</sub>	250	3 (R <sub>g</sub> /R <sub>a</sub> )	No	<20	4000	[60]
Ca-ZnO	Thin film	CO <sub>2</sub>	350	53	Yes	—	50,000	[66]
LFCO-ZnO	Thin film	CO <sub>2</sub>	300	36	Yes	300, 630	2500	This work

**Table 5.**  
Overview of the carbon dioxide sensing characteristics of various thin and bulk materials from literature.

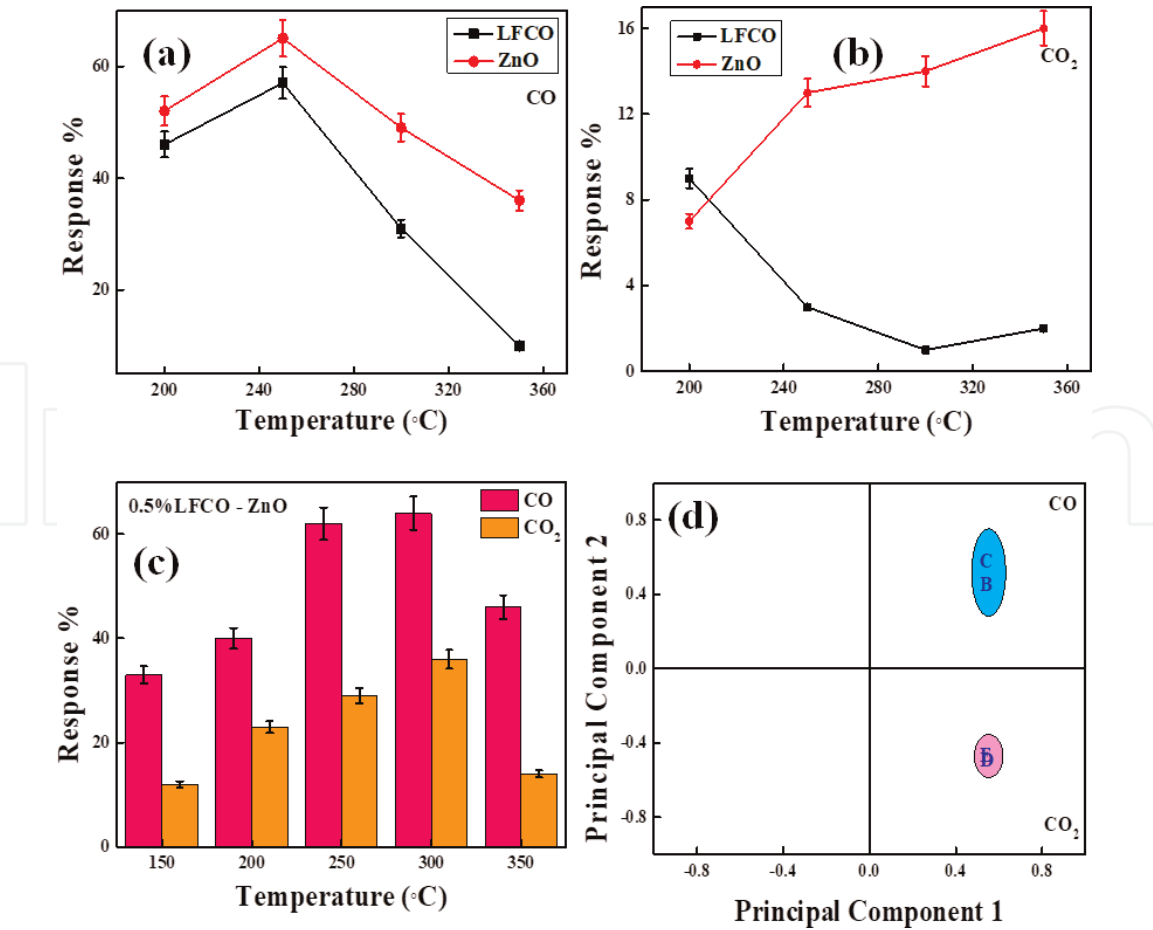


**Figure 14.**  
Temperature variation of response % for pure LFCO and pure ZnO to (a) 500 ppm CO and (b) 2500 ppm CO<sub>2</sub>. (c) Temperature variation of response % of 0.5% LFCO-ZnO for 500 ppm CO and 2500 ppm CO<sub>2</sub>. (d) Principal component analyses for CO and CO<sub>2</sub> at 300°C.

The LFCO-ZnO composite follows the gas sensing behavior of an n-type semiconductor due to the presence of a large number of ZnO crystallites. Therefore, analyses of the conductance transients of CO and CO<sub>2</sub> gases follow Langmuir adsorption mechanism similar to ZnO thin film sensor. Activation energy,  $E_a$ , and heat of adsorption,  $Q$ , have been calculated in accordance with the theory described in the previous section. **Figure 15d** represents the variation of  $E_a$  with concentration for CO and CO<sub>2</sub> gases. It should be noted that each gas possesses distinct activation energy values. The activation energy decreases from 153.83 kJ/mol to 149.67 kJ/mol for 500 ppm CO to 50 ppm CO, whereas the activation energy decreases from 155.93 kJ/mol to 155.28 kJ/mol for 2500 ppm CO<sub>2</sub> to 1000 ppm CO<sub>2</sub>. The variation in  $E_a$  is much less in CO<sub>2</sub> than in CO which could pertain to the efficiency of CO<sub>2</sub> sensing of 0.5% LFCO-ZnO thin film.

As discussed earlier, when the sensor surface is exposed to air, oxygen ions adsorb on the sensor surface which leads to the formation of an electron-depleted layer and hence a potential barrier between two grains. The conductance  $G$  at temperature  $T$  is given by Eq. (12).

Now, assuming Langmuir adsorption (ideal gas), when sensor surface is exposed to gas, it is covered with a monolayer of gas molecules/atoms. The conductance transients are fitted according to Eq. (18) for the response transient. The recovery transient, however, represents decay of conductance, and it is fitted by the following equation:

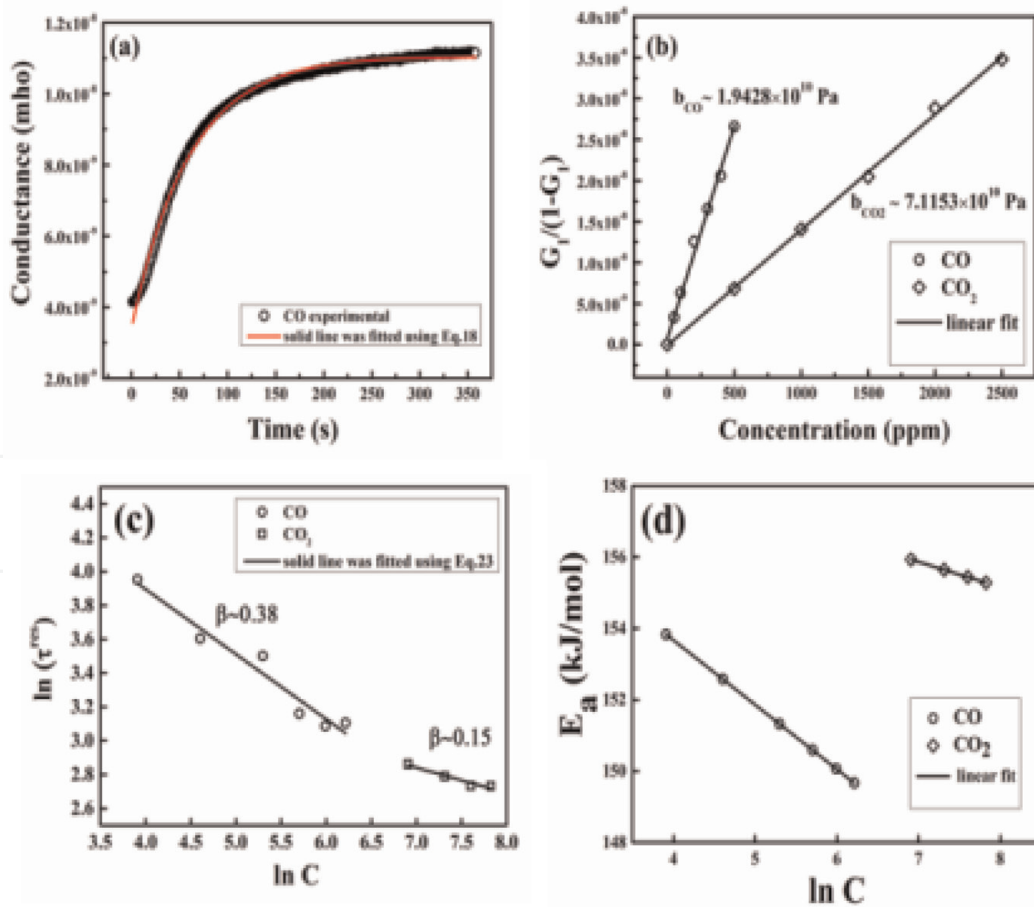


**Figure 15.**

(a) Conductance transient plot for 500 ppm CO sensing. Experimental points are shown by symbols, and the solid line was fitted using Eq. (18), (b) linear variation of  $G/(1-G)$  with concentration, (c) log-log plot of  $\tau^{res}$  with  $C$ . experimental points are shown by symbols, and the solid line was fitted using Eq. (23), (d) variation of  $E_a$  with  $\ln C$  for CO and CO<sub>2</sub> sensing. For all these measurements, operating temperature was kept fixed at 300°C.

$$G(t)_{\text{recovery}} = G'_0 + G \left[ \exp \left( \frac{-t}{\tau_{\text{recovery}}} \right) \right] \tag{51}$$

**Figure 16** shows the conductance transients of CO and CO<sub>2</sub> fitted with Eqs. (18) and (51). **Table 6** summarizes the fitted parameters. Each parameter is unique to both the gases. It may be noted that the response times to both CO and CO<sub>2</sub> are almost similar (~60 and 68 s, respectively) although the response % is markedly different (64 and 36%, respectively).

Assuming nonlinear variation of sheet conductance with test gas concentration, the gas sensing response varies with absolute temperature T according to the following relation:

$$\frac{R_a - R_g}{R_a} = \frac{a_0}{6} \times \exp \left( -\frac{E_a}{RT} \right) \left[ 6 + n.m_0^2 \exp \left( -\frac{E_k}{RT} \right) T^{-0.5} \right] \times \left[ \frac{C_{AS}}{\cosh \left( m_0.\exp \left( -\frac{E}{2RT} \right) T^{-0.25} \right)} \right]^n \tag{52}$$

where  $R_a$  is the resistance in air,  $R_g$  is the resistance in gas,  $a_0$  is the pre-exponential constant,  $n$  is the sensitivity of the gas,  $m_0$  is the Hatta number,  $E_k$  is the activation energy of the first order reaction, and  $C_{AS}$  is the test gas concentration at the film surface [6].

The response (S) versus absolute temperature (T) follows a “bell-shaped” dynamic and can be fitted in accordance with Eq. (52) to yield parameters specific to CO and CO<sub>2</sub>. **Figure 17** shows the S versus T fitting for CO and CO<sub>2</sub>. Sensitivity of the thin film, “n,” is higher for CO<sub>2</sub> which shows that the sensor surface is more active toward CO<sub>2</sub> adsorption. Addition of 0.5% LFCO to ZnO structure enhances

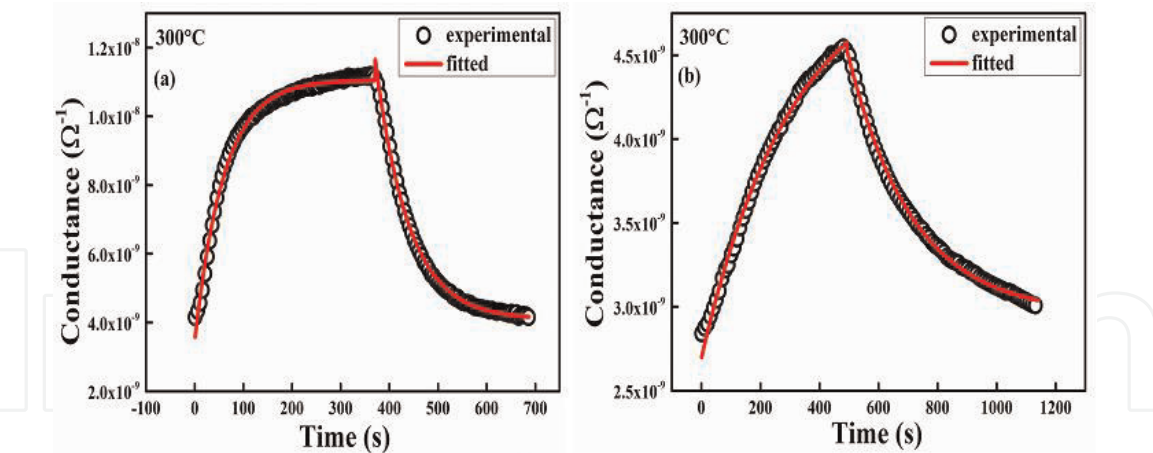


**Figure 16.**  
Fitted conductance transients of (a) CO and (b) CO<sub>2</sub> at 300°C in accordance with Eqs. (18) and (51).

Fitted response parameters	T <sub>opt</sub>	G <sub>0</sub> (Ω <sup>-1</sup> )	G (Ω <sup>-1</sup> )	τ <sub>res</sub> (s)
CO	300 °C	3.45165E-9	7.60875E-9	59.74
CO <sub>2</sub>	300 °C	2.69149E-9	2.34245E-9	303.00
Fitted recovery parameters	T <sub>opt</sub>	G <sub>0</sub> (Ω <sup>-1</sup> )	G (Ω <sup>-1</sup> )	τ <sub>rec</sub> (s)
CO	300°C	4.09001E-9	7.6711E-9	68.56
CO <sub>2</sub>	300°C	2.95542E-9	1.57362E-9	220.29

**Table 6.**  
Fitted parameters for the conductance transients of CO and CO<sub>2</sub> at 300°C.

oxygen adsorption on the ZnO surface due to the formation of additional defects. Also, the formation of multiple junctions in the composite leads to the phenomenon of “band bending” which enhances the interaction of CO<sub>2</sub> with oxygen ions. It may be noted that CO interferes with CO<sub>2</sub> sensing in the composite due to the formation of multiple junctions. This problem is eliminated in the ZnO/LFCO bilayer (not shown) which consists of only a single p-n junction and, thus, is selective to CO<sub>2</sub>.

Simulated parameters from **Figure 17** are summarized in **Table 7** where  $E_a$  and  $E_k$  have units of  $\text{J mol}^{-1}$ . Significant differences may be noted for the simulated parameters of each gas. **Table 7** and **Figure 15d** corroborate the fact that the activation energy is lower for CO which explains the higher response to CO. It may also be emphasized that the parameters are valid for the entire range of operations of the sensor. The simulation may provide useful insights regarding the maximum and minimum temperature at which the sensor is operative. Further, a logarithmic plot of sensor response  $S$  and concentration  $C$  yields a value of  $\sim 0.67$  for CO and  $\sim 1.56$  for CO<sub>2</sub> (**Figure 18**) which is well in agreement with the simulated values. Additionally, it is shown that sensor response decreases sequentially with decreasing concentration as can be seen from **Figure 18**. The limiting concentration for CO is 50 ppm and that for CO<sub>2</sub> is 500 ppm. The detection limit for CO<sub>2</sub> is well above the permissible exposure limit (PEL) which is  $>5000$  ppm. Thus, we may conclude that 0.5% LFCO-ZnO composite thin film is a fair CO<sub>2</sub> sensor and is well suited for practical applications.

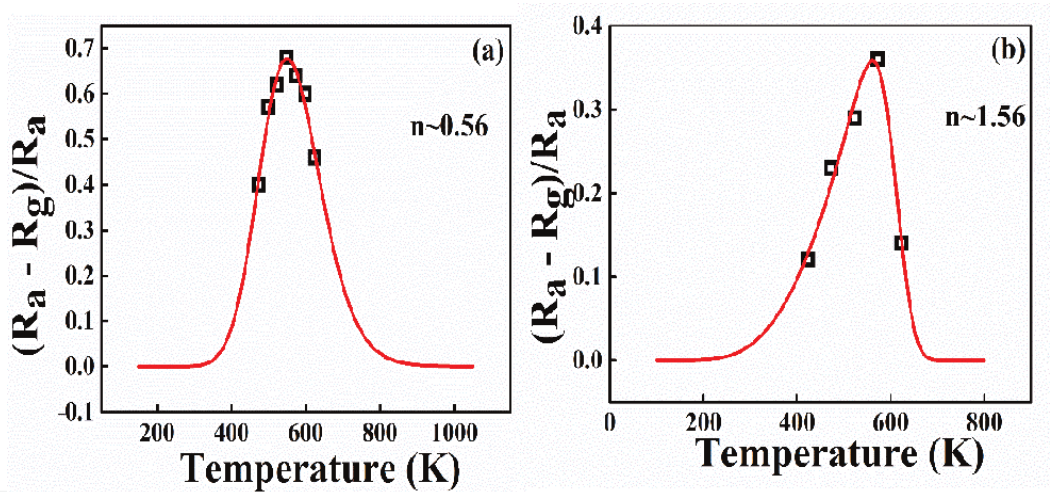


**Figure 17.** Estimated value of sensitivity “ $n$ ” for (a) CO and (b) CO<sub>2</sub> from the fitting of response vs. temperature using Eq. (52).

Fitting parameters	Carbon monoxide	Carbon dioxide
$E_k/R$	3611.87	15674.17511
$a_0/6$	3278.17	1.22219E-5
$E_a/R$	6062.32	2007.15851
$m_0 = L(\sqrt{(k/D_k)})$	1240.78	2.9675E6
$n$ (sensitivity)	0.5654	1.56
$C_{AS}$ (ppm)	500	2500

**Table 7.** Fitted parameters from the fitting of response versus temperature of CO and CO<sub>2</sub>.

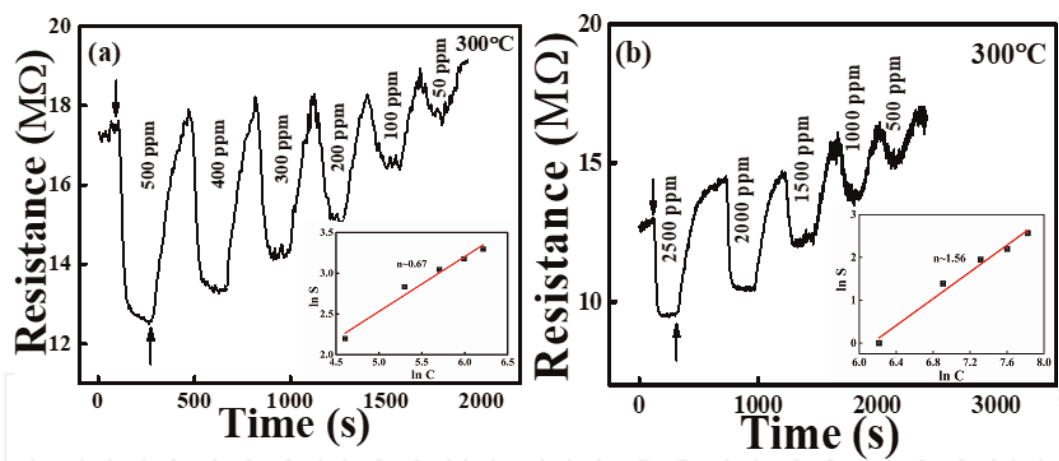
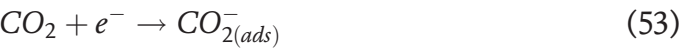


**Figure 18.** Concentration variation in 0.5% LFCO-ZnO for (a) CO (500–50 ppm) and (b) CO<sub>2</sub> (2500–500 ppm); inset in both figures shows logarithmic variation of response with concentration which can be fitted linearly to obtain “n,” the sensitivity.

4.3.1 CO<sub>2</sub> sensing mechanism of LFCO-ZnO thin film gas sensor

The electrical resistance change in ZnO, which is an n-type conducting material, is attributed to adsorption and desorption kinetics of oxygen on ZnO surface. Chemisorption of molecular oxygen of the type O<sub>2</sub><sup>−</sup> occurs above room temperature on ZnO surface, leading to the formation of electron depletion layer (EDL). As the temperature increases up to ~300°C, the molecular oxygen dissociates into atomic form and forms a thicker EDL which pushes inside the ZnO core. Homogeneous particles observed in ZnO thin film microstructure (**Figure 13a**) contribute to the increased rate of oxygen adsorption on ZnO surface. This increases the sensitivity toward CO<sub>2</sub> gas as can be observed from **Figure 14b**. Reaction of carbon dioxide molecules with adsorbed oxygen is given below [68]:

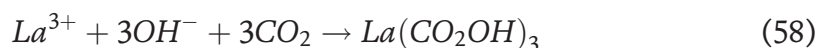
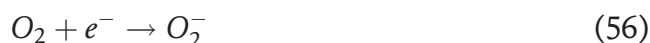


These equations are consistent with the reduction in resistance of ZnO sensor on exposure to CO<sub>2</sub>. In principle, ZnO sensor should register an increase in resistance on exposure to CO<sub>2</sub> as it is an oxidizing gas. However, it was found that ZnO demonstrates typical n-type behavior when brought in contact with CO<sub>2</sub>. This anomaly can be explained from the defect chemistry and catalytic properties of ZnO. This demands a more detailed study and is currently beyond the scope of this book. Thus, we have confined ourselves to the current discussion of LFCO-ZnO composite thin film sensor.

When n-type ZnO is combined with p-type LFCO (LaFe<sub>0.8</sub>Co<sub>0.2</sub>O<sub>3</sub>) sensor, a p-n junction is created at the interface between the two sensors. On exposure to CO<sub>2</sub>, the junction pushes further in to the ZnO core. This leads to an enhanced CO<sub>2</sub> sensing response as compared to pristine LFCO and ZnO sensors.

The general reaction mechanism of LaFeO<sub>3</sub> (LFO) was reported by [69] in which LFO reacts with CO<sub>2</sub> in the presence of moisture to form carbonates. The reaction is given below.





The carbonates thus formed aid in CO<sub>2</sub> sensing by reducing the activation energy required for the reaction to occur. Further, equalization of Fermi levels takes place via migration of carriers leading to the formation of p-n junction. On exposure to CO<sub>2</sub>, hydroxycarbonates form at the junction interface leading to the increase of potential barrier. This increases the concentration of holes at LFCO interface. However, as the concentration of LFCO is only 0.5%, hole accumulation at LFCO surface is impeded, and fall in resistance occurs, and the composite as a whole shows n-type sensing behavior [60].

SnO<sub>2</sub> thick film gas sensor did not show any appreciable CO<sub>2</sub> sensing. This is due to the absence of a Schottky contact in between SnO<sub>2</sub> thick film and silver electrodes. Investigations on CO<sub>2</sub> sensing were not performed for any composite thick film sensor.

#### 4.4 VOC sensing characteristics of thin and thick film

Volatile organic compounds such as ethanol, acetone, and isopropanol pollute auto cabins and indoors of buildings. Long time spent indoors in such an environment ultimately leads to sick building syndrome and also has been found to be linked to leukemia and lymphoma. VOCs are also biomarkers of lung cancer and type 2 diabetes. Ethanol, acetone, and isopropanol have a permissible exposure limit of 1000 ppm over an 8 h work shift as documented by OSHA.

**Figure 19** demonstrates the necessity of VOC detection. Traditionally, n-type semiconducting metal oxides such as SnO<sub>2</sub>, ZnO, WO<sub>3</sub>, TiO<sub>2</sub>, In<sub>2</sub>O<sub>3</sub>, Fe<sub>2</sub>O<sub>3</sub>, etc. have been used for VOC sensing. However, recent research activities show that p-type semiconducting metal oxides such as copper oxide have been gaining popularity in gas sensing mainly due to its ease of fabrication, low cost, high stability, and high response to volatile organic compounds. CuO architectures such as nanorods [70], nanosheets [71], nanoparticles [72], and thin film [19] play an important role in gas sensing behavior. Thin films, in particular, are preferred over powdered CuO variants due to high stability and ease of device fabrication (**Table 8**). Additionally, composites have also gained prominence in selective VOC sensing. We have synthesized CuO thin films using solgel technique. Quartz substrate was used to deposit

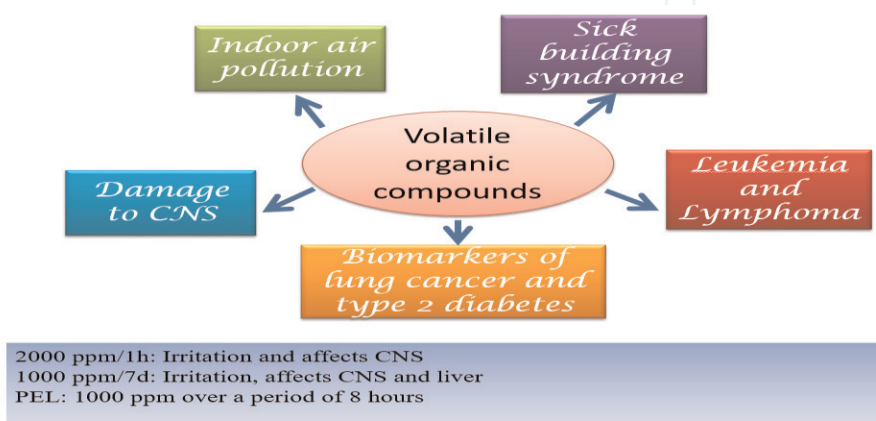


**Figure 19.**  
Permissible exposure limit and harmful effects of volatile organic compounds.

Sensor material	Geometry	Test gas	T <sub>opt</sub> (°C)	S%	τ <sub>res</sub> , τ <sub>rec</sub> (s)	Mixed gas sensing	Conc. (ppm)	Ref.
CuO	Nanowire	n-Propanol	190	6.2	1.2, 6.6	No	100	[76]
CuO	Nanosheets	Ethanol	320	4.22	2–15, 5–24	No	500	[73]
CuO	Thin film	2-Propanol	225	282	12, 279	No	300	[19]
CuO	Nanorods	Ethanol	350	90	—	No	600	[70]
CuO	Nanoparticles	Ethanol	200	5.6	10, 8	No	500	[74]
CuO	Powder	Ethanol	230	2.37 (R <sub>g</sub> /R <sub>a</sub> )	—	No	210	[75, 76]
CuO	Nanoparticles	Ethanol	220	2.7 (R <sub>g</sub> /R <sub>a</sub> )	11, 7	No	0.1	[72]
CuO	Thin film	Ethanol Acetone	300	144 168	3, 216; 7, 248	Yes	300	This work

**Table 8.**  
*Comparison of VOC sensing performances of CuO powders and thin films reported in recent literature.*

the thin films using spin coating. After heat treatment, gold electrodes were deposited on these films using sputter coating following which the gas sensing measurements were performed in a static gas sensing setup. The VOCs were found to be cross-sensitive. Cross-sensitivity was addressed with principal component analysis. Additionally, we have also investigated the VOC sensing characteristics of WO<sub>3</sub>-SnO<sub>2</sub> thick film. Investigations into various thick films for VOC sensing has been tabulated in **Table 9**. The gas–solid interaction in this case was modeled with the Freundlich adsorption isotherm which is nonlinear in nature.

The CuO sensors, thus synthesized, were used for detection of ethanol and acetone by varying the operating temperature (200–300°C) and gas concentration (25–300 ppm). It was found that CuO shows high response and excellent stability with respect to both these gases. The response to 300 ppm acetone and ethanol was found to be 168 and 144%, respectively (**Figure 12**). The response and recovery times were found to be 7 and 248 s for acetone and 3 and 216 s for ethanol, respectively. The static gas sensing setup is similar to a real environment response which explains the delayed recovery times. The response times mentioned are not exact as in a static gas sensing setup, where response to the test gas does not saturate before recovery begins [19]. Mixed gas sensing was also performed with ethanol and acetone (300 ppm/300 ppm) at 300°C. It was found that the response was not affected by the order in which the gases were injected into the static chamber. Principal component analysis was used as a discriminatory method to quantify the gases for mixed gas sensing data (**Table 9**).

4.4.1 Ethanol and acetone sensing mechanism in CuO sensor

CuO is a p-type sensor, and as such the sensing mechanism of a p-type sensor differs slightly to that of an n-type sensor. The major carriers in this case are holes. The concentration of holes changes at the sensor surface due to reaction with the target gas. When the CuO sensor is exposed to air at the operating temperature range of 200–300°C, oxygen takes up electrons from the sensor surface, and the oxygen ions formed chemisorb onto the surface. This increases the density of holes resulting in the decrease of the surface Fermi level. A hole accumulation layer (HAL) at the surface increases the conduction of holes which reduces the baseline

Sensor material	Geometry	Gas	T <sub>opt</sub> (°C)	S %	τ <sub>res</sub> , τ <sub>rec</sub> (s)	Selectivity	Conc. (ppm)	Ref.
CeO <sub>x</sub> - SnO <sub>2</sub>	Thick film	Ethanol	350	95	1.1	Yes	200	[77]
Mg <sub>0.5</sub> Zn <sub>0.5</sub> Fe <sub>2</sub> O <sub>4</sub>	Nanoparticles	Ethanol	325	50	—	No	200	[78]
TiO <sub>2</sub>	Nanoparticles	Ethanol	375	65	—	No	200	[79]
Barium hexaferrite	Nanoparticles	Ethanol	375	90	—	Yes	200	[80]
Sr-SnO <sub>2</sub>	Thick film	Ethanol	300	65	2, 7		100	[81]
SnO <sub>2</sub>	Thick film	Ethanol	300	84	8, 340	Yes	300	[20]
WO <sub>3</sub> -SnO <sub>2</sub>	Thick film	Ethanol	250	73	10, 312	Yes	300	[15]

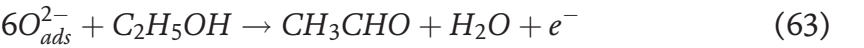
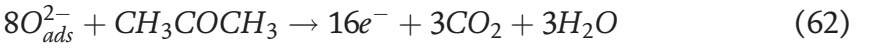
**Table 9.**  
*Comparison of ethanol sensing performances of nanopowders and thick films reported in recent literatures.*

resistance of CuO (R<sub>a</sub> = resistance in air ambient). The equations involved are listed below [19].



On exposure to acetone and ethanol, the oxygen ions react with the test gases to produce carbon dioxide and water with the release of electrons. This process reduces the thickness of the hole accumulation layer which increases the sensor resistance (R<sub>g</sub> = resistance in gas ambient) [75].

The probable reaction mechanisms for acetone and ethanol are



In the end, electron hole recombination takes place and the HAL diminishes.

4.4.2 Mixed gas sensing in CuO thin film sensor and principal component analyses

We have also investigated mixed gas sensing for 300 ppm acetone and 300 ppm ethanol. We found that the mixed gas sensing response (205%) is much higher than individual sensing response of acetone (168%) and ethanol (144%), but it was not an addition of the individual responses (**Figures 20 and 21**). Further, it was found that the order in which the gases were injected into the static chamber had no bearing on the mixed gas sensing response.

This can be attributed to the fact that the gas with the higher reactivity will first interact with the adsorbed O<sup>-</sup> ions, leaving the next gas to react with less number of the same ions leading to reduced sensing [77].

The gases can be discriminated by principal component analyses, which quantify the gases in a multi coordinate system. Fast Fourier transform was utilized to extract the important features of the resistance transients of both acetone and ethanol measured at 300°C. These parameters were then fed into a linear unsupervised principal component analyses pattern recognition technique. **Figure 22a** shows the clustering of ethanol and acetone when injected individually.

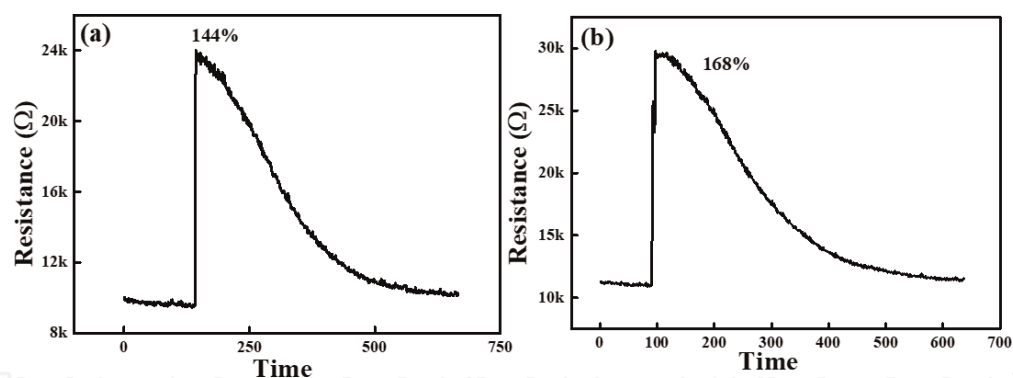


**Figure 20.**  
Resistance transients showing the response % of (a) ethanol and (b) acetone.

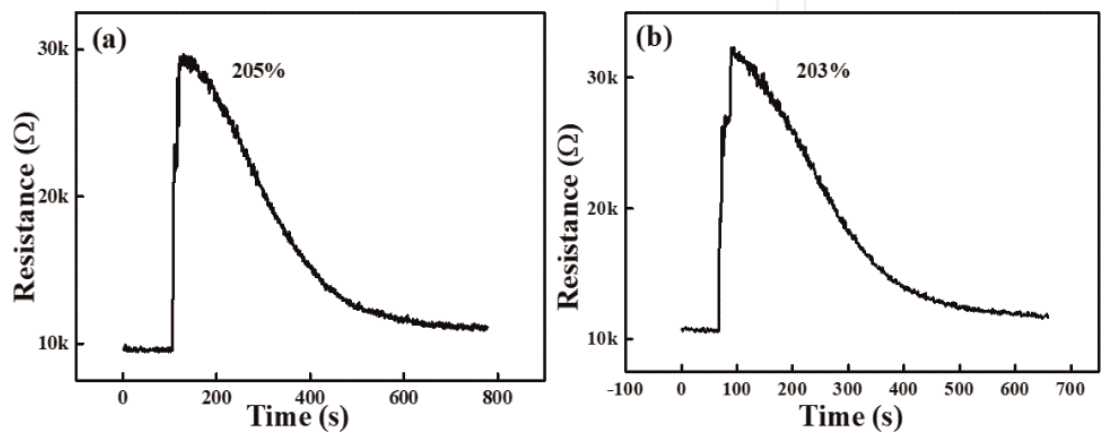


**Figure 21.**  
Resistance transients showing the response % of (a) 300 ppm ethanol and 300 ppm acetone and (b) 300 ppm acetone and 300 ppm ethanol.

The clustering does not change when all the resistance transients of 300 ppm each of acetone and ethanol are analyzed (**Figure 22b**). Thus, PCA can be successfully used to identify the gases in a mixture of acetone and ethanol.

Additionally, we have explored the VOC sensing characteristics of  $\text{WO}_3\text{-SnO}_2$  composite thick film sensor [15]. Sensing measurements were made in the range 300–150°C for 300 ppm ethanol, acetone, and isopropanol. The composite thick film was found to be cross-sensitive to each of the gases. To address the cross-sensitivity, the conductance transients of the gases were further analyzed. These

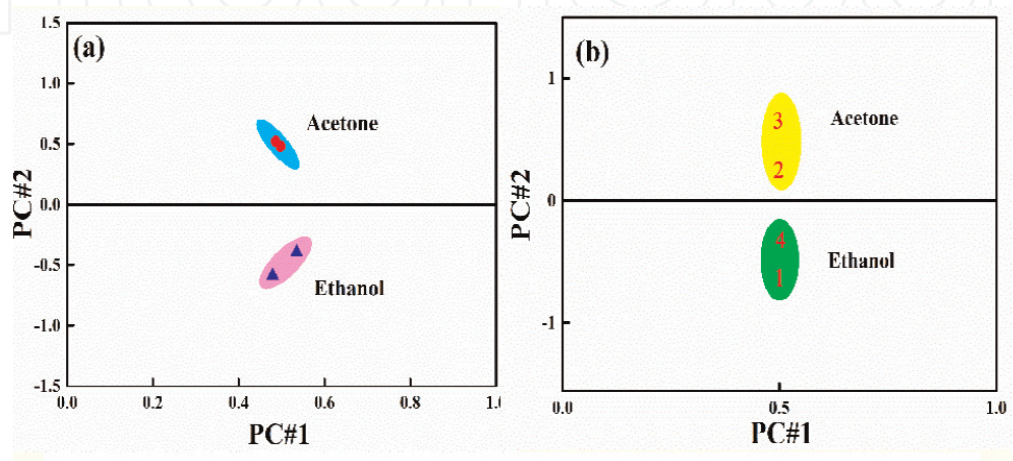


**Figure 22.**  
Principal component analyses for (a) individual gases and (b) mixed gases; note the separate clustering enabling us to distinguish the gases.

conductance transients were obtained at 250°C, and VOC concentration was kept fixed at 300 ppm. Conductance transients for the three VOCs at respective concentration level were fitted using Eq. (18) to estimate the values of parameters such as  $G_0$  (mho),  $G_1$  (mho), and  $\tau^{\text{res}}$  (s). **Figure 23b** envisages the nonlinear variation of  $G_1/(1-G_1)$  with VOC concentration (C) (symbols). In this case, Langmuir adsorption isotherm is not validated since the variation of  $G_1/(1-G_1)$  with concentration is nonlinear for all the gases and does not pass through the origin. In fact, the results are much closer to the Freundlich adsorption isotherm. The relation between  $G_1$  and C in this case obeys the following relation:

$$\frac{G_1}{1-G_1} = \alpha C^\delta \quad (65)$$

From the nonlinear fit, we estimated the values of  $\alpha$  and  $\delta$  for all VOCs under consideration. These results indicate that the sensor surface is not homogeneous and heat of adsorption (Q) is not uniform unlike the Langmuir model.

In case of Langmuir adsorption isotherm, assuming  $Z = G_1/(1-G_1)$ , differentiating Eq. (19) we can write

$$\frac{dZ}{dC} = \frac{1}{b} \quad (66)$$

Differentiating Eq. (66), we can write

$$\frac{dZ}{dC} = (\alpha\delta)C^{\delta-1} \quad (67)$$

Assuming Z vs. C slope at a particular point  $\sim 1/b$ , we can write

$$\frac{1}{b} = (\alpha\delta)C^{\delta-1} \quad (68)$$

$$b = \frac{1}{(\alpha\delta)C^{\delta-1}} = b_0 \exp\left(-\frac{Q}{RT}\right) \quad (69)$$

Simplification of Eq. (69) yields

$$Q = RT [\ln b_0 - (1-\delta) \ln C + \ln \alpha\delta] \quad (70)$$

We have estimated  $b_0$  from the expression given in Eq. (16). Assuming  $\nu = 10^{13}$  Hz [49],  $R = 8.314 \text{ J K}^{-1}$ , and  $T = 523 \text{ K}$ , Eq. (16) can be simplified to.

$$b_0 = 2.7443 \times 10^{-9} \left( \frac{1}{K_0 \cdot S_{\text{area}}} \right) \times M^{1/2} \text{ Pa} \quad (71)$$

As described earlier, considering the surface area,  $S_{\text{area}} \sim 16.2 \text{ \AA}^2$  for nitrogen (molecular weight =  $28 \text{ g mol}^{-1}$ ), we can easily calculate the surface area for ethanol which is  $26.61 \text{ \AA}^2$  (molecular weight =  $46.0 \text{ g mol}^{-1}$ ). Assuming condensation coefficient  $K_0 = 1$  [47], for all test gases,  $b_0$  (at  $T \sim 523 \text{ K}$ ) can be estimated using Eq. (71). From Eq. (70) we have estimated Q as a function of VOC concentration at 250°C.

**Figure 24a** shows the log-log plot of characteristic response time ( $\tau^{\text{res}}$ ) vs. VOC concentration. As shown in **Figure 24a**, variation of  $\tau^{\text{res}}$  with C follows the following relation:

$$\tau^{\text{res}} = \tau_0 \times C^{-\beta} \quad (72)$$

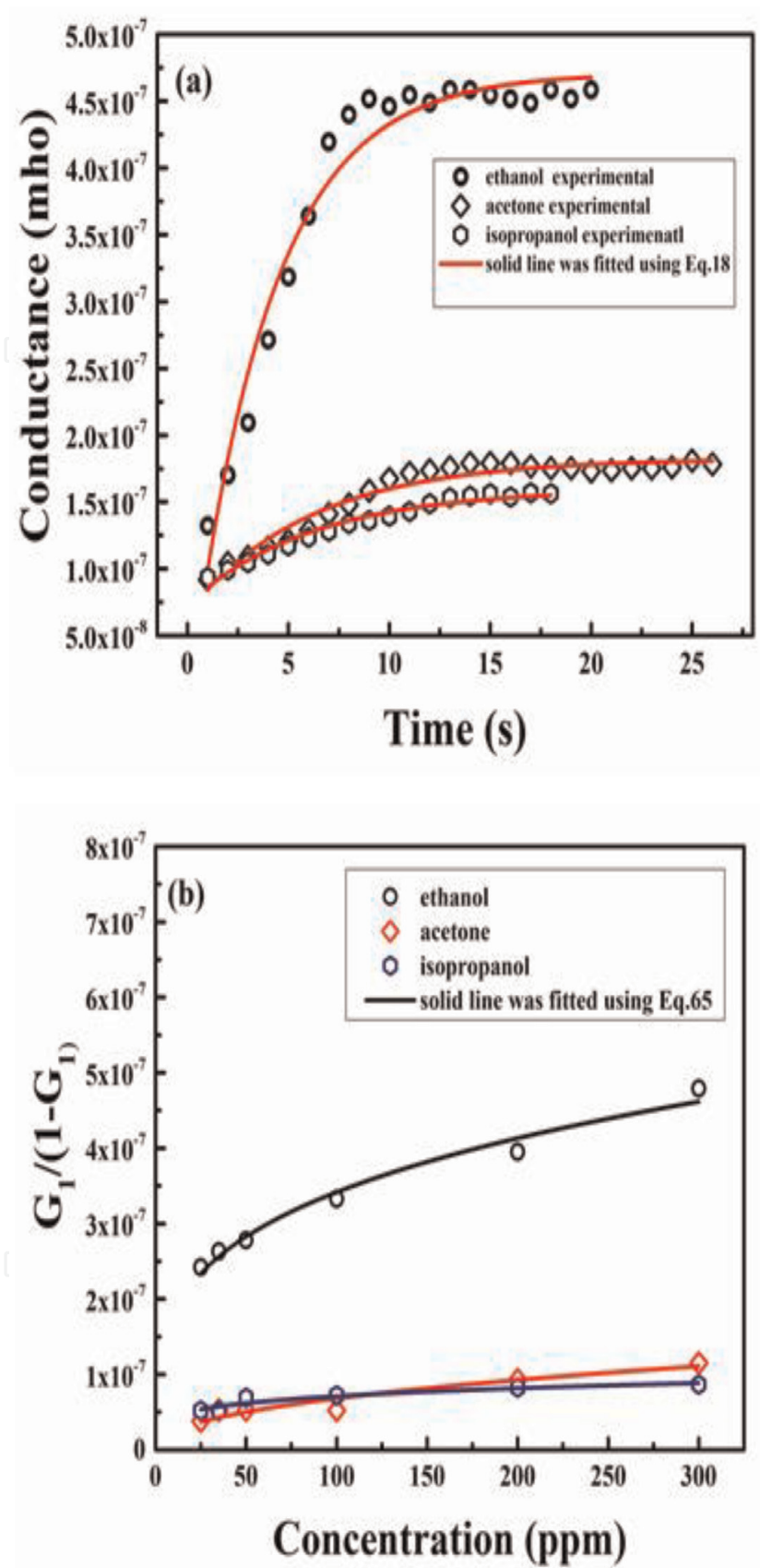


**Figure 23.**  
(a) Conductance transient plots measured at 250°C for 300 ppm ethanol, acetone, and isopropanol sensing. Experimental points are shown by symbols, and the solid line was fitted using Eq. (18), and (b) nonlinear variation of  $G_1/(1-G_1)$  with concentration (ppm). Experimental points are shown by symbols, and the solid line was fitted using Eq. (65) (Figure 23a, b reprinted from [15] with permission from Elsevier).

The  $\ln(\tau^{\text{res}})$  vs.  $\ln(C)$  plot was fitted linearly in order to estimate value of  $\beta$  for three VOCs under consideration.

In case of Freundlich adsorption isotherm, temperature-dependent variation of  $\tau^{\text{res}}$  can be written as per the following relation:

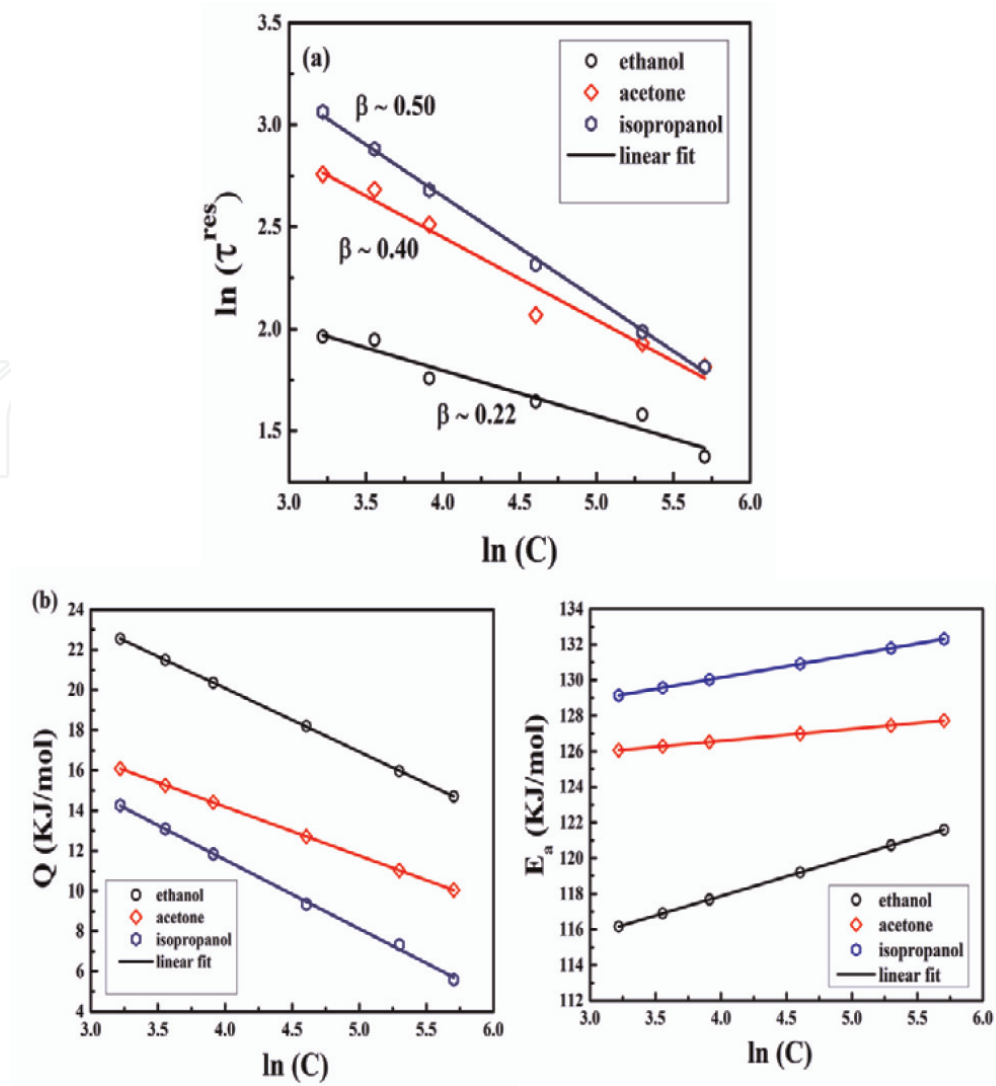


**Figure 24.**

(a) Log-log plot of  $\tau^{res}$  with  $C$ . The sensing measurements were carried out at 250°C, and (b) variation of  $E_a$  and  $Q$  with concentration for ethanol, acetone, and isopropanol sensing (Figure 24a, b reprinted from [15] with permission from Elsevier).

$$\tau^{res} = v^{-1} \times \exp\left(\frac{E_a + Q}{RT}\right) \quad (73)$$

Using Eqs. (70) and (72), we can easily simplify Eq. (73). Activation energy,  $E_a$ , is expressed via the following relation:

$$E_a = RT \times \ln\left(\frac{\tau_0 \cdot v \cdot C^{(1-\delta-\beta)}}{\alpha \cdot \delta \cdot b_0}\right) \quad (74)$$

From Eqs. (70) and (74), we can determine the linearity of  $Q$  versus  $\ln C$  plot as well as the  $E_a$  versus  $\ln C$  plot. Also, we can see that  $Q$  decreases with gas concentration, whereas  $E_a$  shows the exact opposite behavior. Figure 24b shows the variation of  $E_a$  and  $Q$  for each VOC concentration ( $T = 250^\circ\text{C}$ ) [15]. From our analysis, we have estimated that  $E_a$  for ethanol sensing is lower than that of acetone and isopropanol which justify the larger yield of the composite sensor in terms of ethanol sensing ( $S\% \rightarrow \text{ethanol} > \text{acetone} > \text{isopropanol}$ ).

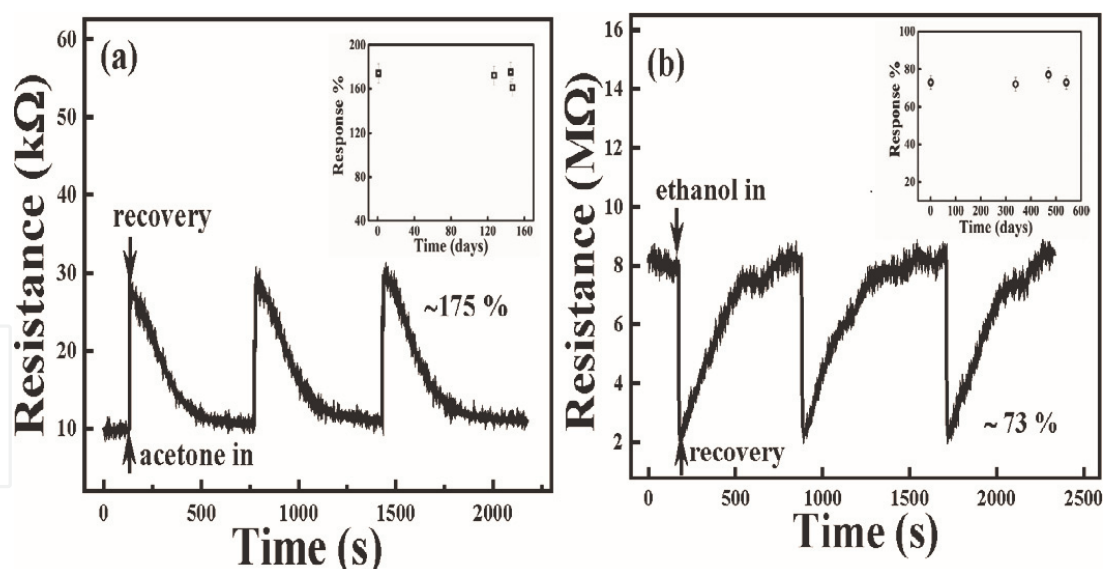


**Figure 25.** Typical resistance transient plots showing reproducibility toward 300 ppm (a) acetone sensing in CuO thin film and (b) ethanol sensing in WO<sub>3</sub>-SnO<sub>2</sub> thick film; inset of each figure shows invariance of response % with time (Figure 25b reprinted from [15] with permission from Elsevier).

#### 4.4.3 Reproducibility of CuO thin film and WO<sub>3</sub>-SnO<sub>2</sub> thick film

The stability and reproducibility of CuO thin film and WO<sub>3</sub>-SnO<sub>2</sub> thick film composite sensors were studied with respect to acetone and ethanol gases (Figure 25). Excellent baseline recovery was achieved for both the sensors for an extended period of time with marginal change of initial response %. The response % for CuO sensor was recorded for a period of ~150 days, whereas that for WO<sub>3</sub>-SnO<sub>2</sub> sensor was recorded for ~500 days. Stable baseline was recorded for CuO thin film sensor, whereas WO<sub>3</sub>-SnO<sub>2</sub> thick film sensor was prone to drift in baseline resistance.

## 5. Conclusions

This chapter throws light on detection of common air pollutants including carbon monoxide, carbon dioxide, nitrogen dioxide, volatile organic compounds, and also hydrogen. The permissible exposure limits for these gases act as benchmark for minimum concentration of gas detection. Gas sensing terminologies such as response %, response time, recovery time, selectivity, and stability have been defined. The interaction of semiconducting metal oxide sensor with reducing gas has been illustrated. Factors that affect the performance of a gas sensor, namely, receptor, transducer, and utility functions, have been explained. It was reported that the receptor function is influenced by the grain size of the sensor. The transducer function controls the flow of charge carriers between the electrodes. It is highly dependent on purity of the sensor material. The utility function controls the diffusion processes of gas during response and recovery processes.

A modified wet chemical route was chosen as the method to synthesize sols required for thin film deposition process. The sols were deposited on quartz and glass substrates and annealed at a high temperature. The materials (ZnO-G, ZnO, SnO<sub>2</sub>, LFCO-ZnO, CuO, and WO<sub>3</sub>-SnO<sub>2</sub>) for gas sensors were chosen after extensive literature review and earlier experiments conducted by us in our laboratory.

High response (894%) to 5 ppm NO<sub>2</sub> sensing was reported for ZnO-G multilayer as compared to pure ZnO (26%) at 150°C. Also, NO<sub>2</sub> detection is selective at 150°C

with respect to 500 ppm each of CO, H<sub>2</sub>, and i-C<sub>4</sub>H<sub>10</sub> gases. The high response and selectivity have been attributed to the presence of p-n junction between ZnO and G grains. The formation of a p-n junction increases the amount of available electrons increasing the gas response. In addition, mixed gas sensing for NO<sub>2</sub>/CO, NO<sub>2</sub>/H<sub>2</sub>, and NO<sub>2</sub>/i-C<sub>4</sub>H<sub>10</sub> has also been reported. Principal component analyses have been demonstrated as an effective tool for the quantification of these mixed gases. ZnO thin film and SnO<sub>2</sub> thick film were investigated for CO and H<sub>2</sub> detection. Both materials demonstrated cross-sensitivity to the gases. Cross-sensitivity was addressed through modeling based on Langmuir adsorption mechanism. Activation energy, E<sub>a</sub>, and heat of adsorption, Q, were calculated based on the model. E<sub>a</sub> and Q values were found to be distinct for each gas and varied as a function of gas concentration. Further, the irreversible nature of ZnO thin film and reversible nature of SnO<sub>2</sub> thick film were demonstrated when exposed to a fixed concentration of CO and H<sub>2</sub> gases. CO<sub>2</sub> sensing characteristics of LFCO-ZnO thin film sensor were investigated. The thin film sensor yields 36% response to 2500 ppm CO<sub>2</sub> at 300°C. LFCO-ZnO thin film is cross-sensitive to CO at this temperature. Principal component analyses have been performed to eliminate cross-sensitivity. Further, Langmuir adsorption mechanism is validated in LFCO-ZnO thin film sensor as the variation of conductance and concentration is a straight line passing through origin (not shown). A model has also been developed for the thin film gas sensor relating response with temperature. Modeling of the response with temperature for CO and CO<sub>2</sub> sensing yielded parameters unique to both gases. Volatile organic compounds have been detected with a CuO thin film sensor. Both acetone and ethanol show high response with a response time of only a few seconds. The gases have been quantified using principal component analyses. Mixed gas (ethanol/acetone) sensing has also been reported for CuO thin film. The mixed gases have been identified on the basis of the PCA cluster for individual gases. WO<sub>3</sub>-SnO<sub>2</sub> thick film sensor was investigated for ethanol, acetone, and isopropanol sensing characteristics. The thick film sensor yielded highest response to 300 ppm ethanol. Freundlich adsorption mechanism was dominant as the variation of conductance and concentration is nonlinear. Based on this adsorption mechanism, E<sub>a</sub> and Q values were estimated for each gas. Both E<sub>a</sub> and Q values were found to vary linearly with gas concentration.

## Acknowledgements

The research work was partially supported by research grant obtained from CSIR, Government of India, vide sanction letter no. 03/(1371)/16/EMR-II, dated 10 May 2016 and NNetRa grant vide sanction 5 (1)/2017-NANO dated 28 March 2018, DST/NM/NNetRa/2018 (G)-IIT-KGP dated 21 March 2018.

## Conflict of interest

The authors declare no conflict of interest.

## Nomenclature

C	concentration
CO	carbon monoxide
CO <sub>2</sub>	carbon dioxide

CuO	copper oxide
$C_g$	reducing gas concentration
EDL	electron depletion layer
$eV_s$	Schottky barrier
$E_a$	activation energy for gas adsorption during response process
$E_d$	activation energy for gas desorption during response process
FFT	fast Fourier transform
$F\theta$	total number of active sites
G	graphene
$G(t)$	conductance transient of the sensor
$G(t)^{response}$	conductance transient of the sensor during response process
$G_0$	conductance of the sensor in air
$G_1$	conductance of the sensor at site 1
HAL	hole accumulation layer
H <sub>2</sub>	hydrogen
k	Boltzmann constant
K	equilibrium constant for response process
$K_0$	fraction of molecules with energy $> E_a$
LFCO	cobalt doped lanthanum ferrite
M	molar mass of gas
MEA	methanolamine
MO	metal oxide
MOE	methoxyethanol
NMP	N-methyl-2-pyrrolidine
NO <sub>2</sub>	nitrogen dioxide
$N_A$	Avogadro number
$N(t)$	number of gas molecules adsorbed at time t
$N^*$	total number of available adsorption sites
OSHA	Occupational Safety and Health Administration
$O_{ads}^-$	chemiadsorbed oxygen
$O_{ad-surface}$	physiadsorbed oxygen
P	gas pressure
PCA	principal component analysis
PEL	permissible exposure limit
Q	heat of adsorption
R	universal gas constant
$R_a$	sensor resistance in air
$R_{ad}$	physiadsorbed reducing gas
$R_g$	sensor resistance in reducing gas
$RO_{ad}$	adsorbed oxidizing product of reducing gas
$RO_{gas}$	desorbed oxidizing product of reducing gas
S	sensor response (%)
$S_{area}$	surface area of a single adsorbed molecule
$S_p$	sensor response (%) of p-type semiconductor
$S_n$	sensor response (%) of n-type semiconductor
SMO	semiconducting metal oxide
SnO <sub>2</sub>	tin oxide
$T_{opt}$	operating temperature of sensor
VOC	volatile inorganic compound
WO <sub>3</sub>	tungsten oxide
ZnO	zinc oxide
$\kappa$	selectivity factor

$\nu$	frequency of oscillation of adsorbed gas
$\tau_{irrev}$	characteristic response time in irreversible response process
$\tau_{rev}$	characteristic response time in reversible response process
$\tau_{res}$	response time of sensor
$\tau_{rec}$	recovery time of sensor

Author details

Tyneer Bhowmick<sup>1</sup>, Vibhav Ambardekar<sup>2</sup>, Abhishek Ghosh<sup>3</sup>, Moumita Dewan<sup>1</sup>, Partha Pratim Bandyopadhyay<sup>2</sup>, Sudip Nag<sup>4</sup> and Subhasish Basu Majumder<sup>1\*</sup>

1 Materials Science Centre, Indian Institute of Technology, Kharagpur, India


2 Mechanical Engineering, Indian Institute of Technology, Kharagpur, India

3 Department of Biomedical Engineering, University of Michigan, USA

4 Electronics and Electrical Communication Engineering, Indian Institute of Technology, Kharagpur, India

\*Address all correspondence to: subhasish@matssc.iitkgp.ac.in

IntechOpen

© 2020 The Author(s). Licensee IntechOpen. Distributed under the terms of the Creative Commons Attribution - NonCommercial 4.0 License (<https://creativecommons.org/licenses/by-nc/4.0/>), which permits use, distribution and reproduction for non-commercial purposes, provided the original is properly cited. 

## References

- [1] Zampolli S, Elmi I, Ahmed F, Passini M, Cardinali GC, Nicoletti S, et al. An electronic nose based on solid state sensor arrays for low-cost indoor air quality monitoring applications. *Sensors and Actuators B: Chemical*. 2004;**101**:39-46
- [2] World Health Organization. Household Air Pollution and Health. Weblog. Available from: <https://www.who.int/news-room/fact-sheets/detail/household-air-pollution-and-health>. 2018
- [3] United States Department of Labour. OSHA Annotated PELs—Occupational Safety and Health Administration. Weblog. Available from: <https://www.osha.gov/dsg/annotated-pels/tablez-1.html>. 2019
- [4] Bhargav KK, Ram S, Labhsetwar N, Majumder SB. Correlation of carbon monoxide sensing and catalytic activity of pure and cation doped lanthanum iron oxide nano-crystals. *Sensors and Actuators B: Chemical*. 2015;**206**: 389-398
- [5] Mukherjee K, Majumder SB. Analyses of response and recovery kinetics of zinc ferrite as hydrogen gas sensor analyses of response and recovery kinetics of zinc ferrite as hydrogen gas sensor. *Journal of Applied Physics*. 2009;**106**:064912
- [6] Ghosh A, Majumder SB. Modeling the sensing characteristics of chemi-resistive thin film semi-conducting gas sensors. *Physical Chemistry Chemical Physics*. 2017;**19**: 23431-23443
- [7] Ambardekar V, Bandyopadhyay PP, Majumder SB. Hydrogen sensing performance of atmospheric plasma sprayed tin dioxide coating. *International Journal of Hydrogen Energy*. 2019;**44**(26): 14092-14104
- [8] Mukherjee K, Gaur APS, Majumder SB. Investigations on irreversible and reversible-type gas sensing for ZnO and  $\text{Mg}_{0.5}\text{Zn}_{0.5}\text{Fe}_2\text{O}_4$  chemi-resistive sensors. *Journal of Physics D: Applied Physics*. 2012; **45**(50):505306
- [9] Bhowmick T, Banerjee A, Nag S, Majumder SB. Gas sensing characteristics in ZnO thin film explicated through the analysis of conductance transients and the concept of activation energy. *Proceedings of IEEE Sensors. INSPEC Accession Number 18329455*. 2018. DOI: 10.1109/ICSENS.2018.8589612
- [10] Barsan N, Weimar U. Conduction model of metal oxide gas sensors. *Journal of Electroceramics*. 2001;**7**(3): 143-167
- [11] Kim H, Lee J. Highly sensitive and selective gas sensors using p-type oxide semiconductors: Overview. *Sensors and Actuators B: Chemical*. 2014;**192**: 607-627
- [12] Kalisadhan M. Gas sensing characteristics of wet chemical synthesized spinel ferrites [PhD dissertation]. Kharagpur: Materials Science Centre, Indian Institute of Technology, Kharagpur; 2011
- [13] Bochenkov VE, Sergeev GB. Chapter 2: Sensitivity, selectivity, and stability of gas-sensitive metal-oxide nanostructures. In: *Metal Oxide Nanostructures and Their Applications*. Vol. 3. Valencia, California, USA: American Scientific Publishers; 2010. pp. 31-52. Available from: <http://www.chem.msu.su/rus/books/2011/sergeev/all.pdf>
- [14] Ghosh A, Bhowmick T, Majumder SB. Multi-layered zinc oxide-graphene composite thin films for selective nitrogen dioxide sensing.

Journal of Applied Physics. 2018;**123**: 084501

[15] Ambardekar V, Bandyopadhyay PP, Majumder SB. Understanding on the ethanol sensing mechanism of atmospheric plasma sprayed 25 wt.% WO<sub>3</sub>-75 wt.% SnO<sub>2</sub> coating. Sensors and Actuators B: Chemical. 2019;**290**: 414-425

[16] Ghosh A, Schneller T, Waser R, Majumder SB. Understanding on the selective carbon monoxide sensing characteristics of copper oxide-zinc oxide composite thin films. Sensors and Actuators B: Chemical. 2017;**253**: 685-696

[17] Korotcenkov G. Chapter 5: Conductance transient analyses of metal oxide gas sensors for the example of spinel ferrite gas sensors. In: Mukherjee, Kalisadhan, Majumder SB, editors. Chemical Sensors: Simulation and Modeling. Volume 1: Microstructural Characterization and Modeling of Metal Oxides. New York, USA: Momentum Press; 2012. Available from: <http://www.momentumpress.net/books/chemical-sensors-simulation-and-modeling-volume-1-microstructural-characterization-and-modelin>

[18] Maity A. Development of nano-structured ceramic oxide gas sensing system for air quality monitoring [PhD dissertation]. Kharagpur: Materials Science Centre, Indian Institute of Technology, Kharagpur; 2015

[19] Ghosh A, Maity A, Banerjee R, Majumder SB. Volatile organic compound sensing using copper oxide thin films: Addressing the cross sensitivity issue. Journal of Alloys and Compounds. 2017;**692**:108-118

[20] Ambardekar V, Bandyopadhyay PP, Majumder SB. Atmospheric plasma sprayed SnO<sub>2</sub> coating for ethanol detection. Journal of Alloys and Compounds. 2018;**752**(2):440-447

[21] Sriskandan K, Pettingale KW. Numismatist's pneumonitis. A case of acute nitrogen dioxide poisoning. Postgraduate Medical Journal. 1985;**61**: 819-821

[22] CBC. 'Inadequate Ventilation' at Super 8 led to Carbon Monoxide Poisoning, Officials say. CBC News [Newspaper on the Internet]. July 10, 2019. Available from: <https://www.cbc.ca/news/canada/manitoba/carbon-monoxide-poisoning-hotel-winnipeg-super8-1.5206755> [Cited: July 30, 2019]

[23] Permentier K, Vercammen S, Soetaert S, Schellekens C. Carbon dioxide poisoning: A literature review of an often forgotten cause of intoxication in the emergency department. International Journal of Emergency Medicine. 2017;**10**(14):17-20

[24] Kumarvel V, Da Fonseca J. Acetone poisoning—A diagnostic dilemma. EJA. 2007;**24**:803-816

[25] Dilisi GA. Disaster: Combining physics and history in the laboratory. Physics Teacher. 2017;**55**:268-273

[26] Jacob K. Nitrogen Emissions Going Up: Study. The Hindu [Newspaper on the Internet]. June 6, 2018. Available from: <https://www.thehindu.com/sci-tech/energy-and-environment/nitrogen-emissions-going-up-study/article24090131.ece> [Cited: July 30, 2019]

[27] Zhang J, Wang S, Wang Y, Wang Y, Zhu B, Xia H, et al. NO<sub>2</sub> sensing performance of SnO<sub>2</sub> hollow-sphere sensor. Sensors and Actuators B: Chemical. 2009;**135**(2):610-617

[28] Lee D, Nam K, Lee D. Effect of substrate on NO<sub>2</sub>-sensing properties of WO<sub>3</sub> thin film gas sensors. Thin Solid Films. 2000;**2**:142-146

[29] PCKKJ L. NO<sub>2</sub> sensing characteristics of ZnO nanorods

prepared by hydrothermal method. *Journal of Electroceramics*. 2006;**2**: 975-978

[30] Neri G, Bonavita A, Galvagno S, Siciliano P, Capone S. CO and NO<sub>2</sub> sensing properties of doped-Fe<sub>2</sub>O<sub>3</sub> thin films prepared by LPD. *Sensors and Actuators B: Chemical*. 2002;**82**(2): 40-47

[31] Srivastava S, Jain K, Singh VN, Singh S, Vijayan N, Dilawar N, et al. Faster response of NO<sub>2</sub> sensing in graphene-WO<sub>3</sub> nanocomposites. *Nanotechnology*. 2012;**23**:205501

[32] Zhang H, Feng J, Fei T, Liu S, Zhang T. SnO<sub>2</sub> nanoparticles-reduced graphene oxide nanocomposites for NO<sub>2</sub> sensing at low operating temperature. *Sensors and Actuators B: Chemical*. 2014;**190**(2):472-478

[33] Maity A, Majumder SB. NO<sub>2</sub> sensing and selectivity characteristics of tungsten oxide thin films. *Sensors and Actuators B: Chemical*. 2015;**206**(2): 423-429

[34] Hübner T, Boon-Brett L, Black G, Banach U. Hydrogen sensors—A review. *Sensors and Actuators B: Chemical*. 2011;**157**(2):329-352

[35] Gal M. Enhanced optical detection of hydrogen using the excitation of surface plasmons in palladium. *Applied Surface Science*. 1993;**68**:135-138

[36] Jamnani SR, Moghaddam HM, Leonardi SG, Donato N, Neri G. Applied surface science synthesis and characterization of Sm<sub>2</sub>O<sub>3</sub> nanorods for application as a novel CO gas sensor. *Applied Surface Science*. 2019;**487**: 793-800

[37] Hou L, Zhang C, Li L, Du C, Li X, Kang X, et al. CO gas sensors based on p-type CuO nanotubes and CuO nanotubes: Morphology and surface

structure effects on the sensing performance. *Talanta*. 2018;**188**:41-49

[38] Chung W, Sakai G, Shimanoe K, Miura N. Preparation of indium oxide thin film by spin-coating method and its gas-sensing properties. *Sensors and Actuators B: Chemical*. 1998;**46**:139-145

[39] Singh A, Sharma A, Tomar M, Gupta V. Growth of highly porous ZnO nanostructures for carbon monoxide gas sensing. *Surface and Coating Technology*. 2018;**343**:49-56

[40] Pati S, Maity A, Banerji P, Majumder SB. Qualitative and quantitative differentiation of gases using ZnO thin film gas sensors and pattern recognition analysis. *The Analyst*. 2014;**139**(7):1796

[41] Pati S, Banerji P, Majumder SB. n- to p- type carrier reversal in nanocrystalline indium doped ZnO thin film gas sensors. *International Journal of Hydrogen Energy*. 2014;**39**(27): 15134-15141

[42] Brunet E, Maier T, Mutinati GC, Steinhauer S, Köck A, Gspan C, et al. Comparison of the gas sensing performance of SnO<sub>2</sub> thin film and SnO<sub>2</sub> nanowire sensors. *Sensors and Actuators B: Chemical*. 2012;**165**:110-118

[43] Drmoseh QA, Yamani ZH, Hossain MK. Hydrogen gas sensing performance of low partial oxygen-mediated nanostructured zinc oxide thin film. *Sensors and Actuators B: Chemical*. 2017;**248**:868-877

[44] Chang S. Oxygen chemisorption on tin oxide: Correlation between electrical conductivity and EPR measurements. *Journal of Vacuum Science and Technology*. 2002;**17**(1):366-369

[45] Lenaerts S, Roggen J, Maes G. FT-IR characterization of tin dioxide gas sensor materials under working conditions. *Spectrochimica Acta Part A*:

Molecular and Biomolecular Spectroscopy. 1995;**51**(5):883-894

[46] Mirzaei A, Leonardi SG, Neri G. Detection of hazardous volatile organic compounds (VOCs) by metal oxide nanostructures-based gas sensors: A review. *Ceramics International*. 2016; **42**(14):15119-15141

[47] Hu H, Trejo M, Nicho ME, Saniger JM, García-Valenzuela A. Adsorption kinetics of optochemical  $\text{NH}_3$  gas sensing with semiconductor polyaniline films. *Sensors and Actuators B: Chemical*. 2002;**82**(1):14-23

[48] Mukherjee K, Majumder SB. Analyses of conductance transients to address the selectivity issue of zinc ferrite gas sensors. *Electrochemical and Solid-State Letters*. 2010;**13**:J25

[49] Adamson AW. *Physical Chemistry of Surfaces*. New York, USA: Wiley; 1982. pp. 519-523

[50] Special Correspondent. India's Carbon Dioxide Emissions up 5%. The Hindu [Newspaper on the Internet]. March 27, 2019. Available from: <https://www.thehindu.com/sci-tech/energy-and-environment/indias-carbon-dioxide-emissions-up-5/article26646376.ece54> [Cited: July 30, 2019]

[51] NASA. Global Patterns of Carbon Dioxide. Weblog. Available from: <https://earthobservatory.nasa.gov/images/82142/global-patterns-of-carbon-dioxide>. 2013

[52] Maruyama T, Sasaki S, Saito Y. Potentiometric gas sensor for carbon dioxide using solid electrolytes. *Solid State Ionics*. 1987;**23**:107-112

[53] Shimizu Y, Komori K, Egashira M. Carbon dioxide sensor consisting of  $\text{K}_2\text{CO}_3$ -polyethylene glycol solution supported on porous ceramics. *Journal of the Electrochemical Society*. 1989; **136**(8):2256-2260

[54] Ishihara T, Kometani K, Mizuhara Y, Takita Y. A new type of  $\text{CO}_2$  gas sensor based on capacitance changes. *Sensors and Actuators B: Chemical*. 1991;**5**:97-102

[55] Hoefer U, Kuhner G, Schweizer W, Sulz G, Steiner K. CO and  $\text{CO}_2$  thin-film  $\text{SnO}_2$  gas sensors on Si substrates. *Sensors and Actuators B: Chemical*. 1994;**22**:115-119

[56] Ishihara T, Kometani K, Mizuhara Y, Takita Y. Capacitive-type gas sensor for the selective detection of carbon dioxide. *Sensors and Actuators B: Chemical*. 1993;**14**:470-472

[57] Mizuno N, Yoshioka T, Kato K, Iwamoto M.  $\text{CO}_2$  sensing characteristics of  $\text{SnO}_2$  element modified by  $\text{La}_2\text{O}_3$ . *Sensors and Actuators B: Chemical*. 1993;**14**:473-475

[58] Haeusler A, Meyer JS. A novel thick film conductive type  $\text{CO}_2$  sensor. *Sensors and Actuators B: Chemical*. 1996;**34**:388-395

[59] Yeob D, Kang H, Choi N, Hyun K, Lee H. A carbon dioxide gas sensor based on cobalt oxide containing barium carbonate. *Sensors and Actuators B: Chemical*. 2017;**248**:987-992

[60] Zhang W, Xie C, Zhang G, Zhang J, Zhang S. Porous  $\text{LaFeO}_3/\text{SnO}_2$  nanocomposite film for  $\text{CO}_2$  detection with high sensitivity. *Materials Chemistry and Physics*. 2017;**186**: 228-236

[61] Juang F, Chern W, Chen B. Carbon dioxide gas sensing properties of  $\text{ZnSn}(\text{OH})_6$ - $\text{ZnO}$  nanocomposites with  $\text{ZnO}$  nanorod structures. *Thin Solid Films*. 2018;**660**(March):771-776

[62] Gómez L, Galeano V, Parra R, Michel CR, Paucar C, Morán O. Carbon dioxide gas sensing properties of ordered oxygen deficient perovskite

- LnBaCo<sub>2</sub>O=(Ln= La,Eu). Sensors and Actuators B: Chemical. 2015;**221**: 1455-1460
- [63] Joong H, Han D, Ho J, Zhou Z. Carbon dioxide gas sensor using a graphene sheet. Sensors and Actuators B: Chemical. 2011;**157**(1):310-313
- [64] Herrán J, Mandayo GG, Castaño E. Semiconducting BaTiO<sub>3</sub>-CuO mixed oxide thin films for CO<sub>2</sub> detection. Thin Solid Films. 2009;**517**(22):6192-6197
- [65] Dhahri R, Leonardi SG, Hjiri M, El Mir L, Bonavita A, Donato N, et al. Enhanced performance of novel calcium/aluminum co-doped zinc oxide for CO<sub>2</sub> sensors. Sensors and Actuators B: Chemical. 2017;**239**:36-44
- [66] Ghosh A, Zhang C, Zhang H, Shi S. CO<sub>2</sub> sensing behavior of calcium-doped ZnO thin film: A study to address the cross-sensitivity of CO<sub>2</sub> in H<sub>2</sub> and CO environment. Langmuir. 2019;**35**: 10267-10275
- [67] Kim S, Na CW, Hwang I, Lee J. One-pot hydrothermal synthesis of CuO – ZnO composite hollow spheres for selective H<sub>2</sub>S detection. Sensors and Actuators B: Chemical. 2012;**168**:83-89
- [68] Martinez L, Holguin-Momaca JT, Karthik TVK, Olive-Mendez SF, Campos-Alvarez J, Agarwal V. Sputtering temperature dependent growth kinetics and CO<sub>2</sub> sensing properties of ZnO deposited over porous silicon. Superlattices and Microstructures. 2016;**98**:8-17
- [69] Goldsmith J, Ross S. Factors affecting the infra-red spectra of some planar anions with D<sub>8h</sub> symmetry-III. The spectra of rare-earth carbonates and their thermal decomposition products. Spectrochimica Acta. 1967;**23A**: 1909-1915
- [70] Bhuvaneshwari S, Gopalakrishnan N. Room temperature ammonia and VOC sensing properties of CuO nanorods. AIP Conference Proceedings. 2016;**1731**: 050112-1-050112-3
- [71] Yan H, Tian X, Ma F, Sun J. CuO nanoparticles fabricated by direct thermo-oxidation of sputtered Cu film for VOCs detection. Sensors and Actuators B: Chemical. 2015;**221**: 599-605
- [72] Wang F, Li H, Yuan Z, Sun Y, Chang F, Deng H, et al. A highly sensitive gas sensor based on CuO nanoparticles synthesized via a sol-gel method. RSC Advances. 2016;**6**(83): 79343-79349
- [73] Yan H, Tian X, Sun J, Ma F. Enhanced sensing properties of CuO nanosheets for volatile organic compounds detection. Journal of Materials Science: Materials in Electronics. 2014;**26**(1):280-287
- [74] Yan H, Tian X, Ma F, Sun J. Chemical CuO nanoparticles fabricated by direct thermo-oxidation of sputtered Cu film for VOCs detection. Sensors and Actuators B. 2015;**221**:599-605
- [75] Xia S, Zhu H, Cai H, Zhang J, Yu J, Tang Z. Hydrothermally synthesized CuO based volatile organic compound gas sensor. RSC Advances. 2014;**3**: 57975-57982
- [76] Tan J, Dun M, Li L, Zhao J, Li X, Hu Y, et al. Self-template derived CuO nanowires assembled microspheres and its gas sensing properties. Sensors and Actuators B: Chemical. 2017;**252**:1-8
- [77] Kotchasak N, Wisitsoraat A, Tuantranont A, Phanichphant S, Yordsri V, Liewhiran C. Highly sensitive and selective detection of ethanol vapor using flame-spray-made CeO<sub>x</sub>-doped SnO<sub>2</sub> nanoparticulate thick films. Sensors and Actuators B: Chemical. 2018;**255**:8-21
- [78] Karmakar M, Das P, Pal M, Mondal B, Majumder SB, Mukherjee K.

Acetone and ethanol sensing characteristics of magnesium zinc ferrite nano-particulate chemi-resistive sensor. *Journal of Materials Science*. 2014;5766-5771

[79] Das P, Mondal B, Mukherjee K. Simultaneous adsorption-desorption processes in the conductance transient of anatase titania for sensing ethanol: A distinctive feature with kinetic perception. *Journal of Physical Chemistry C*. 2017;121:1146-1152

[80] Karmakar M, Mondal B, Pal M, Mukherjee K. Acetone and ethanol sensing of barium hexaferrite particles: A case study considering the possibilities of non-conventional hexaferrite sensor. *Sensors and Actuators B: Chemical*. 2014;190: 627-633

[81] Shaikh FI, Chikhale LP, Mulla IS, Suryavanshi SS. Synthesis and enhanced ethanol sensing performance of nanostructured Sr doped SnO<sub>2</sub> thick film sensor. *Journal of Materials Science: Materials in Electronics*. 2017;28(4): 3128-3139